Version 8 january 11th 2004

Main results of the second international PIV Challenge.

M. Stanislas[1], K. Okamoto[2], C. J. Kähler[3] and J. Westerweel[4]

1 Laboratoire de Mécanique de Lille, UMR 8107, Cité Scientifique,
   59655 Villeneuve d'Ascq Cedex France
2 The University of Tokyo, Dept. Quantum Enrg. Systems Sci.,
   7-3-1 Hongo, Tokyo, 113-8656, Japan
3 Institut für Strömungsmechanik, TU Braunschweig, Bienroder Weg 3,
   38106 Braunschweig, Germany
4 Delft University of Technology, Laboratory for Aero & Hydrodynamics,
   Leeghwaterstraat 21, 2628 CA Delft, the Netherlands

e-mail: pivnet-sig32@univ-lille1.fr
Challenge web site: www.pivChallenge.org

Abstract

This paper presents the main results of the second international PIV Challenge which took place in Busan (Korea) on the 19th & 20th of September 2003. This workshop was linked to the PIV03 International Symposium which was held at the same place the following week. The present contribution gives the objectives of the Challenge, describes the test cases and the algorithms used by the participants, and presents the main results together with some discussion and conclusions on the accuracy and robustness of various PIV and PTV algorithms. As all the results obtained cannot be detailed, this contribution should serve as a guide for the use of the full database of images and results which is available at http://www.pivChallenge.org.

Keywords: PIV, PTV, PIV algorithms, accuracy, spatial resolution.

1 Introduction

In September 2001, the first international PIV Challenge took place in Göttingen (Germany), linked to the PIV01 Symposium. This workshop, which was the result of several different cooperative projects, both in Europe and Japan, was a great success. A total of 15 different teams participated in the analysis and about 50 participants were present at the workshop to discuss the results. These results were synthesised by Stanislas et al (2003) and are available on the Challenge website: http://www.pivChallenge.org. Below we only recall the main general conclusions; the reader is referred to the above mentioned paper for further details.

The first point which came out clearly was the overall agreement of the state-of-the-art PIV algorithms, even in regions where difficulties could be expected.

Concerning PTV, the results appeared to be more sensitive to the different algorithms. It was clearly shown that PTV is complementary to PIV, with its ability to cope with low and medium concentration, to reach a higher spatial resolution and to cope with specific cases like regions with

strong velocity gradients. The issue of accuracy assessment was left open, together with a detailed and precise comparison between PIV and PTV.

The work performed for the Challenge was considered interesting enough to be made available to the public via the Challenge website. This was done both to help assessing the performances of new algorithms and second to help newcomers to PIV to validate whether they correctly handle the software they use.

The final general conclusion was that this first experience should be taken into account to prepare a next Challenge, with a smaller number of test cases, carefully selected to investigate specific limitations of the method for turbulence assessment and the camera noise effect.

Following the success of this first Challenge, a second Challenge was initiated by the steering committee. This second Challenge started in September 2002 and was concluded by a workshop linked to the PIV03 Symposium in Busan (Korea). The aim of this second edition was thus to go ahead in the quantitative characterisation of existing PIV and PTV algorithms, taking the lessons learned from the first experience.

On the European side this activity was supported by the PivNet 2 European network (Task 5) and the ERCOFTAC Special Interest Group on PIV (SIG 32), while on the Japanese side the activity was supported by the Japanese Standard Image Project of the Visualization Society of Japan.

2 Organisation

The second Challenge was organised following the same structure as the first edition. A scientific committee was in charge to supervise the scientific aspects while a steering committee was in charge of the practical organisation. The scientific committee for this Challenge is given in Table 1, while the steering committee was composed of the authors of the present paper. The local organisation was taken in charge by the Korean Visualisation Society and the Steering Committee acknowledges here the friendly and efficient help of Professor Kim and his team.

The Challenge web site was established in September 2000. It is managed by Dr Okamoto. It was used for the distribution and collection of images and data for this second Challenge. The Challenge was organised around three selected test cases, which will be presented in detail below. The results from the contributors were presented and discussed during the Busan workshop on September 19th & 20th 2003. The aim was to undertake a detailed and quantitative comparison of the merits of the different evaluation algorithms and software that are available or under development at the contributors to analyse single exposed PIV & PTV images.

Procedure :

A database of PIV records was provided for analysis to the "contributors". All images in this database were single exposed and suitable for cross correlation analysis. They were provided in the TIFF image format as "sets" of two images, referenced 1 and 2 for each exposure.

This database was organised in one package. The full analysis of this package was mandatory to be considered as a "contributor" at the final workshop. This package was composed of 3 test cases that

are given in Table 2. The images were distributed on April 15, 2003 for cases A and B and May 12, 2003 for case C; All results were due on May 19, 2003.

The comparison of the results obtained by the different contributors was performed and presented at the workshop by the steering committee. Data were provided by the contributors as:

- the post-processed displacement fields with spurious vectors removed, but without any interpolation and/or filtering (clean definition in the first Challenge)
- the coordinates at which the displacements are determined,
- a flag matrix giving the location of the points where no correlation was obtained and where spurious vectors were removed.

All results were given in pixel units with the origin at the center of the lower left corner pixel of the image (i.e., (0.5, 0.5) pixels from the lower left corner of the image).

3 Algorithms

A total of 15 contributors participated to the Challenge utilizing both PIV and PTV (see Table 3). Most participants were using PIV, but the PTV participants, although not numerous, had fairly different algorithms.

In order to be able to compare the different features of the evaluation methods applied to the analysis of the Challenge images, the main implementations will be briefly described in the following section and summarized in Table 4a for PIV. For details the reader is addressed to the references listed at the end.

FOI - The team from FOI (Sweden) uses a MATLAB-based evaluation program with a low-pass Gaussian filter for the images to eliminate high-frequency noise. The algorithm uses a multi-grid cross-correlation approach. A three-point Gaussian peak fit is used for the determination of the particle image displacement with sub-pixel accuracy. A specific validation algorithm has been designed. No publication is available on the FOI algorithm.

DUTAE - The evaluation program WIDIM (Window deformation iterative multi-grid) primarily developed at VKI (Scarano & Riethmuller 2000) has been further improved since the previous Challenge (Stanislas et al 2003) at the Delft University Aeronautical Department (Netherlands) (Scarano 2002). The first step included in WIDIM is an iterative multi-grid window deformation method. It allows a de-coupling between the spatial resolution and the dynamic range by using an iterative evaluation procedure with integrated window refinement. The refinement is possible as the in-plane loss-of pairs is compensated almost completely by means of local window shifting and deformation. The deformation is performed symmetrically with respect to the measurement position in order to obtain a 2nd order accurate estimate of the particle image displacement. The image deformation technique is implemented to compensate for the loss-of-pairs due to in-plane velocity gradients, which enhances the signal strength. Image interpolation at sub-pixel positions is performed by the cardinal sine scheme function. The image deformation field is obtained by a linear interpolation of the velocity field. The super-resolution is obtained in a second step by direct measurement of the displacement second spatial derivatives and 2nd order correction of the displacement (SR-WIDIM).

PURDUE - The software package EDPIV applied by Purdue University (USA) (Wereley & Gui 2002) can also be characterized as an iterative 2nd order accurate central difference interrogation (CDIC), which supports continuous window shifting and image deformation methods. The evaluation time can be reduced by FFT acceleration techniques. The peak fitting is a standard 3 point Gaussian fit. For difficult images, a 3×3 smoothing filter with an appropriately-sized unsharp mask is used to form a band-pass filter eliminating both high and low frequency noise in the image. Four or five iterations are necessary to achieve an accurate evaluation with this method.

CORIA 1 - Since the last Challenge (Stanislas et al 2003), CORIA, at Rouen University (France), has developed a multi-grid, multi-pass iterative approach including a whole-symmetric image deformation method. The evaluation of velocity fields at each step of the deformation is based on FFT and includes a continuous window shifting technique (Lecordier & Trinité 2004). It is also possible to rotate the interrogation window in order to align it with the local velocity vector. For the peak fitting, a 2D Gaussian algorithm on a 3x3 points matrix is used.

URS - The software developed by University of Rome together with INSEAN (Italy) (Di Florio et al 2002) is based on weighting (by a 2D Gaussian), re-shaping and re-orientating the interrogation windows. This weighting procedure is applied recursively together with that used to determine the optimal window offset and does not require any window deformation. The peak fitting is a standard 3-point Gaussian fit.

LAVIS - The Lavision Company (Germany) is using its standard commercial package available in version 6 of Davis and based on the method proposed by Scarano & Riethmuller (2000). This is a multi-pass algorithm with adaptive window deformation. Preprocessing based on filtering was applied to certain images. Cyclic FFT was used to compute the spatial correlation. The peak fitting algorithm is the standard 3-point Gaussian fit. A local median filter was used to remove spurious vectors.

UDN - The University of Napoly (Italy) has developed an algorithm based on a multi-grid iterative procedure with deformation of both images (Cardone et al 2002), which is very near to the algorithm of DUTAE. Different weighting functions can be applied to the interrogation window. The peak in the cross-correlation map is interpolated by using either a standard Gaussian fit over the nearest five points or an iterative Gaussian fit over the nearest nine points.

IOT - The Institute of Thermophysics of Novosibirsk (Russia) used a multi-pass multi-grid algorithm with continuous window shifting and no window deformation. The peak fitting algorithm was the standard 3-point Gaussian fit. Validation and smoothing were based on a moving average filter.

DANTEC - The Dantec Company (Denmark) used an adaptive and iterative window deformation algorithm. A high accuracy (sub-pixel) peak fitting algorithm that is independent of the particle image shape and correlation peak shape and specific to the Dantec algorithm was also used. The high accuracy is achieved by using the full information in the correlation function and not just the nine highest values in the correlation plane.

DLR - DLR (Germany) used preprocessing based on high-pass filtering and/or dynamic histogram equalization (Willert 2004). The algorithm was based on a multi-pass multi-grid method with image deformation which is very near to that of the CORIA-1 algorithm . A special feature is the down-sampling of the image instead of using larger interrogation windows. This down-sampling is performed by summing up the intensities of neighboring pixels. Interpolation is based on a cubic B-spline. The peak fitting is a 2D Gaussian fit on a 7×7 matrix.

OSAPREF - The Prefecture University of Osaka (Japan) is using an iterative PIV technique in which the iterative cross-correlation technique and sub-pixel displacement assessment based on the use of the gradient method (Sugii et al 2000) are combined.

LIMSI - The algorithm used by LIMSI-CNRS in Orsay (France) is an orthogonal dynamic programming algorithm (ODP-PIV), developed by Quénot et al (1998). It is based on the search of a transformation that relates the second image to the first by assuming that the intensity is conserved during the displacements and that the displacement of each image point (pixel) is small, rectilinear, uniform and continuous. In a hierarchical processing scheme the global image-to-image transformation is found by minimizing the Minkowski distance between the images. After a successful evaluation, this method provides a displacement vector for each pixel, but it should be mentioned that this method is significantly slower (on the computational point of view) as compared to conventional correlation based methods.

TSI - The TSI Compagny (USA) used their standard commercial INSIGHT software package . This is a multi-pass adaptive integer-window shifting algorithm with a 3-point bilinear peak fitting algorithm.

As can be seen, a variety of algorithms were present, coming both from PIV providers and from leading PIV developing teams. Among those, several algorithms, including multi-pass, multi-grid and image deformation methods, were present. In the present paper, following the current practice of the PIV community, these algorithms will globally be called "advanced algorithms", although a more precise nomenclature would be worth (algorithms including window deformation techniques could be called 2nd order as compared to 1st order window shifting techniques and 0th order correlation techniques without shift) but is beyond the scope of the present paper. Table 4 summarises the main features of these algorithms together with some typical parameters used by the participants for the analysis of the Challenge images.

As far as PTV is concerned, the participation was not so numerous, although fairly different and complementary algorithms were represented. Table 4b summarises the PTV algorithms.

CORIA 2 - The second team from CORIA (France) used a two-step algorithm (Susset et al 2003). In the first step, a standard multi-pass, multi-grid PIV algorithm is applied to construct a predictor of the velocity field. In a second step, a field partitioning iterative approach is used, based on the predicted velocity field, to find the couples of individual particle images.

LAVIS-PTV - The Lavision Compagny (Germany) also used the PIV data (LAVIS) as a predictor. Particle-image detection is performed using a gray-value threshold in combination with a low pass filter. The individual particle displacements are found by applying a correlation algorithm on 16×16

interrogation windows centered on each first exposure particle image. The existence of a particle image at the proper position in the second exposure is validated.

<u>VKI</u> - In the VKI (Belgium) algorithm, the particle extraction is based on the intensity level threshold (Stitou & Riethmuller 2001). The threshold value is determined using the local intensity distribution. The particle tracking is again a hybrid of a cross-correlation and a tracking method. Initially the velocity distributions at grid points are calculated using the WIDIM cross-correlation method (Scarano & Riethmuller 2000). Based on the velocity at the interrogation grid, the particle matching is carried out. A double 3-point Gaussian fit is used to determine the particle image positions. To reduce the probability of mismatching, each particle-image displacement is compared with those in its direct neighborhood.

<u>OSAK</u> - The algorithm of Osaka University (Japan) is a so called pure Particle Tracking Technique (Ohmi & Hang Yu 2000). They extract the particle location using an adaptive threshold technique in combination with low-pass filtering. Then, based on the particle-image location, they tracked the particle image while taking into consideration the displacement magnitude and angle.

4 Case A

The purpose of Case A was to have some actual PIV images, as opposed to idealised synthetic PIV images, of a turbulent flow. This provides the opportunity to test the performances of different algorithms for images taken from an actual experiment in which the tracer particles are not mono-disperse, the particle images are not perfectly Gaussian, the intensity profiles of the two laser pulses are not identical, and the images contain background and random noise components. One of the inherent problems of using actual PIV data is that the true velocity field is unknown, which makes it difficult to determine the actual measurement accuracy. It was therefore decided to use data from a self-similar turbulent jet, for which the turbulence statistics are well known (Rajaratnam 1976). This is a challenging test case, as the observed flow contains both regions of high velocity and high turbulence intensity (near the jet centreline) and regions of low velocity and a laminar flow state (in the outer flow region). One of the main characteristics of a turbulent jet is that the axial momentum flux is a conserved quantity, so there exists a direct relation between the spreading rate of the jet and the entrainment rate of fluid from the outer flow region into the jet. Therefore, despite the fact that the true instantaneous velocity fields are unknown, it was possible to define a critical test of the performance of the PIV interrogation algorithms based on this conserved quantity.

For Case A we used a set of 100 PIV image pairs taken from a submerged turbulent round jet. The working fluid is water, which was seeded with small (5 µm) tracer particles. The jet Reynolds number is $Re = 2 \times 10^3$, and the camera observes a 45×45 mm^2 area with its centre at a distance of 80 mm from the nozzle. The tracer particles are illuminated with a 1 mm thick light sheet, created from the beam of a dual-cavity frequency-doubled pulsed Nd:YAG laser. The particle images are diffraction limited, and estimated to be of the order of one pixel. A detail of one of the PIV image frames is shown in Figure 1. The experiment was originally designed for optimal interrogation with 32×32-pixel interrogation regions, but the seeding density is sufficient for interrogation with 16×16-pixel (or even smaller) interrogation windows, with the use of proper multi-pass and window shifting algorithms. Additional details on the optical configuration and experimental conditions are given by Fukushima *et al.* (2002). The camera (Kodak ES-1.0) has a resolution of 992×1004 pixels

with an 8-bit dynamic range. During the experiment, 12 series of 64 image pairs at 15 Hz frame rate were recorded, which finally yielded a set of 657 image pairs. From this set, a sub-set of 100 randomly selected image pairs were selected for this PIV challenge. This was a compromise between a number large enough to yield reliable turbulence statistics and a number small enough to be manageable for distribution among the challenge participants. A typical result for the interrogation of image pair fj001 and the mean displacement field obtained by averaging all 100 data fields are shown in Figure 2. The jet flow is from right to left with a typical centreline displacement between −6.6 and −3.5 pixels, and a mean jet half width between 96 (on the right) and 193 pixels (on the left).

All participants submitted their final results, and each participant was given the liberty to apply any post-interrogation validation with replacement of spurious vector data. However, it appeared that not all participants performed a post-interrogation validation of the results and labelled the data (see Table 5). In order to test the effectiveness of the post-interrogation evaluation all displacement data for each participant was plotted, and then all data that fell outside the ellipse shown in Figure 3 was counted. The results are listed in Table 5 under 'outliers'. This shows that in most cases the spurious displacements were detected and replaced effectively. Table 5 also lists the percentage of labelled (i.e., 'discarded') data and 'outliers'. In most cases this percentage is well below 1% (for CORIA 1, CORIA 2, DLR, DUTAE, IOT, LAVIS, LIMSI, PURDUE and VKI); for a smaller number of participants (DANTEC, FOI, OSAPREF, TSI and UDN) the percentage is between 1 and 10%, and for two participants (OSAK and URS) the percentage is larger than 10%. In all cases the labelled data and 'outliers' are removed and in case of equidistant PIV data replaced (by the steering committee) by means of the 3×3 local mean. It also appeared that the VKI data were represented in a mirrored frame of reference, which was corrected by a multiplication of all data in the vertical direction with −1. Then the PIV vector data were ensemble averaged, and the 2D mean displacement field was fitted by means of a least-squares method to:

$$U(x-x_0, y-y_0) = U_c(x)\exp\left[-\left(y-y_0\right)^2/\ell(x)^2\right] \quad \text{with}: \begin{cases} U_c(x) = A/(x-x_0) \\ \ell(x) = B \cdot (x-x_0) \end{cases}, \tag{1}$$

where (x_0, y_0) is the virtual jet origin, U_c the mean centreline velocity, ℓ the mean jet width, and B the jet spreading rate. The fitted values for A and B are listed in Table 5. With these fitted parameters the velocity data and radial position are scaled by U_c and ℓ respectively, so that all instantaneous data can be averaged and represented as a single one-dimensional profile.

The results for the scaled mean axial velocity are shown in Figure 4. This shows that the data from all participants generated the same self-similar profile. However, the results for the scaled radial profiles, shown in Figure 5, are quite different. This is especially visible in the outer flow region, where the displacements are only about 2% percent of the centreline velocity. The results for $\eta < -2$ range from 0.01 U_c to 0.02 U_c, which is a 100% variation of the results. Note that the variation of the results for $-2 < \eta < 2$ is much smaller; this region corresponds to the central jet region where the turbulence intensity is high. Apparently, the measurement in the turbulent flow region is more accurate than in the laminar flow region! This is a remarkable result; the mean value of the displacements in the laminar region (where the velocity fluctuations are nearly zero) are of the same magnitude as the mean value of the displacements in the turbulent region (where the magnitude of the velocity fluctuations are an order of magnitude larger than the mean displacement). The situation in the laminar flow region closely corresponds to a test case in which a test pattern is uniformly displaced over a small distance (less than a pixel), whereas the situation in the turbulent

7

flow region would correspond to a test case with a strongly non-uniform fluctuating component; therefore it is strange that the non-uniform region with large fluctuations yields a more coherent result than the uniform, non-fluctuating region. Evidently, the laminar, low-velocity flow region is a challenging flow. The variation in the PTV results for the self-similar radial velocity profile is much larger; in particular the results from OSAK and VKI do not appear to reveal the correct profile. Although the displacements are small and so are the absolute errors, the precise measurement of the radial velocity is an important aspect as it is directly related to the entrainment of outer fluid into the turbulent jet. This will be discussed in more detail at the end of this section.

The profiles for the axial and radial turbulence intensities are also self-similar in the measurement domain (Fukushima *et al.* 2002), and the results for the scaled axial turbulence intensities are shown in Figure 6. In general the data from all participants resolve the shape near the jet centreline, but the differences appear in the outer flow region where the displacements are small and the turbulence level is low. Details of the graphs in Figure 6 are shown in Figure 7. As the turbulence level in the outer flow region is zero, these results would reveal the rms displacement error. It appears that the results from the PIV data occur in three groups, which is clearly related to the dimensions of the interrogation domain: DUTAE, LAVIS, PURDUE and UDN use 32×32-pixel interrogation domains, and obtain an rms error of 0.010–0.018 U_c, which corresponds to an rms displacement error of 0.07–0.12 px. This value is in good correspondence to the rms displacement error reported for 32×32-pixel interrogation domains and 3-point Gaussian sub-pixel interpolation (Westerweel *et al.* 1996; Westerweel *et al.* 1997; Westerweel 2000). CORIA 1 and DANTEC use small interrogation domains (16×16 and 24×24-pixels, respectively), and consequently have a larger rms error of about 0.028 U_c, which corresponds to an rms displacement error about 0.18 px. This value is in correspondence with the theoretical estimate (Westerweel 1997, 2000). However, DLR and LIMSI also use interrogation domains that are smaller than 32×32 pixels, but the rms error is not significantly larger than that of the 32×32-pixel interrogation result. FOI, IOT, TSI and URS use 32×32-pixel interrogation domains, and obtain an error of about 0.008 U_c, which corresponds to an rms displacement error of about 0.05 px. This is in correspondence to the theoretical prediction for the optimal performance of 32×32-pixel interrogation domain with a 3-point Gaussian fit (Westerweel 2000a,b). It is not clear whether the lower rms is due to post-interrogation smoothing (as reported by IOT), which could also explain a reduced rms error. The PTV results of CORIA 2 show rms errors comparable to 32×32-pixel PIV interrogation, whereas the OSAK, LAVIS-PTV and VKI results seem to be of the same order as the '16×16'-pixel PIV interrogation results.

One of the issues in PIV interrogation is the displacement mean bias error, i.e. so-called 'peak locking' in which the measured displacements are biased towards integer pixel values (Westerweel 2000b). In Figure 8 the histograms for the axial displacement are plotted for displacements between −8 and 0 pixels are plotted, and in Figure 9 are plotted the normalised histograms of the fractional displacements. There is quite a difference in the degree of peak locking, despite the fact that for all algorithms identical data was used. The degree of 'peak locking' was quantified by taking the standard deviation of the histogram values, which is listed in Table 5. For the PIV data in Figure 9 there appears to be two main groups. The first group includes CORIA 1, DLR, DUTAE, FOI, LAVIS, LIMSI and UDN and the second group includes DANTEC, IOT and TSI. The peak locking parameter is between 0.0012 and 0.0020 for the first group and about 0.003 for the second group. The histogram for the first group can be understood in terms of the theoretical histogram, based on the linear correspondence of the rms displacement error as a function of the displacement for the three-point Gaussian fit (Westerweel *et al.* 1997; Westerweel 2000). When a uniform distribution

for the true fractional displacement is assumed, the expected histogram can be easily computed by means of a Monte-Carlo integration; given a 0.1 px rms error for a ±0.5 px displacement, the expected histogram value at ±0.5 px displacement is 0.83, which corresponds quite well with the histograms for the first group. In the case of a 0.2 px rms error for a ±0.5 px displacement, the expected histogram value at ±0.5 px displacement is 0.56; this corresponds well with the results for the second group. This implies that the histograms for the fractional displacement for CORIA 1, DANTEC, DLR, DUTAE, FOI, IOT, LAVIS, LIMSI, PURDUE, TSI and UDN can be explained in terms of the existing theoretical statistical properties of the 3-point Gaussian sub-pixel interpolation. The result from PURDUE is remarkable as it shows an almost uniform distribution for the fractional displacement, i.e. no peak locking is observed. The corresponding peak-locking parameter is very low (0.0007; see Table 5). As reported, PURDUE uses a window shifting method in which both interrogation windows are shifted symmetrically with respect to the interrogation position. This appears to effectively eliminate the peak locking effect, although it should be mentioned that the symmetrical window shifting could generate a 'modulo 2' peak locking effect (this was not further investigated), and that others who also claim to use symmetrically offset interrogation windows display peak locking. It is unclear why OSAPREF and URS show much stronger peak locking in comparison to the other results. The PTV results, with the exception of the LAVIS PTV data, show a very strong peak locking effect, which is undoubtedly due to the fact that the particle images are smaller than two pixels in diameter (Westerweel 2000b). The appearance of the OSAK data is due to the fact that they rounded off all data to 1 digit after the decimal point. The results of LAVIS PTV show that they use a sub-pixel interpolation method that does not suffer from significant peak locking, despite the small particle-image diameter.

We now return to the differences in the mean radial velocities in the outer flow region of the jet. The displacements in this region are about one percent of the mean centreline velocity, i.e. of the order of 0.10–0.15 pixels, and therefore the measurement accuracy very much depends on the proper implementation of the PIV interrogation algorithm and properties of the sub-pixel interpolation method. Also, there exists a direct relationship between the jet spreading rate B (listed in Table 5) and the radial velocity in the outer flow region, i.e. the entrainment velocity (Rajaratnam 1976); the measured mean radial velocity should be in accordance with the measured jet spreading rate. Hence, the evaluation of the mean radial velocity in the outer jet region provides an excellent test on both the accuracy and (in particular) the internal consistency of the interrogation results. Rather than computing the expected radial velocity from the (observed) spreading rate B, a more direct method was used. Recall that the original data comprise of 15 Hz time series. This makes it possible to find for each image pair (I_1,I_2) a subsequent image pair (I_3,I_4) taken 66.7 ms later. So, apart from the image pair (I_1,I_2), taken with a 1.2 ms time delay, we have an additional image pair (I_1,I_4) taken with a 67.9 ms time delay. This means that the displacement in the outer flow region for the (I_1,I_4) image pair is about 57 times larger, yielding displacements in the range of 5–8 pixels which can be measured with a precision of 0.1–0.2 pixels. These measurements can be used to provide an accurate value for the entrainment velocity. When the data are averaged over all 100 image pairs and re-scaled to the original 1.2 ms time delay, this yields a estimate for the displacement with a precision better than 4×10^{-4} px. A 150×50-pixel region on the right side of the image at about 375 pixels from the jet centreline was used to determine the mean radial velocity. The results are shown in Figure 10 in conjunction with the precisely measured result with a value around 0.13 px. When we look at these results, we can see a large variation in the results of more than 50%. This is remarkable in view of the results for the spreading rate B in

9

Table 5, which differ by less than 4% (if we ignore the OSAK result). Most results under-estimate the entrainment velocity, with the exception of those of PURDUE and DUTAE for the PIV and LAVIS PTV for the PTV who over-estimate the entrainment velocity. It is interesting to note that the results of LAVIS and LIMSI almost coincide, which is also the case for the results of IOT and TSI. This may be due to similarities in the interrogation algorithms. It is unclear why OSAPREF and OSAK show a profile with the opposite trend.

5 Case B

The images for case B were generated from a DNS simulation of a turbulent open channel flow provided by Prof. Tsubokura of the Tokyo Electro-communication University. A total of 49 million points were used for this high resolution simulation (576×576×148). The Reynolds number based on the channel half width and the wall friction velocity was Re_τ (= hu_τ/v) = 640. To compute the flow, the following parameters were chosen: U_{max} = 1.19 m/s, u_τ = 34.1 mm/s, h = 300 mm, v = 16 mm^2/s (air). With these values, the visualised area was: y^+ = 0–100, x^+ = 1–300. With this field size, 1 pixel corresponds to 0.195 wall units, which would be a fairly good spatial resolution for a PIV experiment in such a configuration. The time separation was adjusted to keep the out-of-plane motion smaller than 1/2 of the thickness of the laser light sheet. Following Foucaut et al (2004), this leads to about 12% of loss of particle image pairs due to the out-of-plane motion, which is fairly challenging based on the criteria by Keane & Adrian (1990). The strongest velocity gradient (near the wall) was about 1.5 times the particle image diameter using a 32×32-pixel interrogation window. Following Keane & Adrian (1992), this is far above the optimum for standard PIV (which should be 0.5 in order to limit the deformation of the correlation peak). In this region the optimum interrogation window size would be 10×10 pixels. The particle motion is calculated based on the velocity data that were interpolated in 3D space and in time. The displacement is integrated with short time step, i.e., 1×10^{-6} sec. The PIV images were generated using the Japanese standard image generator (Okamoto et al., 2000a,b , http://www.piv.jp/). Figure 11 gives an example of a small region of 150×150 pixels from image B001a. The average particle image diameter d_p is 1.3 pixels at one standard deviation and 2.6 pixels at two times the standard deviation (The standard deviation being 0.65 pixel). This is near to the optimum particle-image diameter for PIV. The particle images have a Gaussian shape. The camera fill ratio was set at 0.3, which is a bit less than standard PIV cameras, but this is not a very sensitive parameter. The particle image source density, defined as N_S = C.πd^2/4, was 0.09, so speckle effects can safely be ignored. This leads to an optimal interrogation window size of 12×12 pixels with on average 10 particle image pairs per window (Keane & Adrian 1990).

Each contributor uploaded the 100 velocity maps to the Challenge web site. The DNS data were interpolated on a 4×4-pixel uniform grid using a 4D linear interpolation. This allowed a point-by-point comparison for each velocity map with the data of all contributors. The steering committee did the comparison and produced all the plots that will be discussed hereafter. To maintain the clearity of the graphs, given the large number of contributors, the data were split into three groups: two groups for PIV and one for PTV (the classification was based on the registration list). For conciseness, the results will not always be shown for all groups. Sometimes, the most representative group will be chosen for a particular graph. The interested reader is referred to the Challenge

website, where all the results are available, for further details. All the results are given in pixel units.

Figure 12 shows the comparison of the mean velocity profile with the DNS data for the first PIV group. The results of the second PIV group and the PTV group are very similar. As can be seen, except for the very first points near the wall, the agreement is very good between the different teams. This near wall region is enlarged in Figure 13 for both PIV groups and the PTV teams. In PIV, only two teams have a first grid point at a distance of 4 pixels from the wall: LAVIS and CORIA. All the others have their first interrogation position at 8 pixels from the wall, using generally 16×16-pixel interrogation windows (IW). The scatter of the measured displacement at this first data point (which is the maximum scatter in the field) is of the order of ± 0.3 pixels, which is at an acceptable level taking into account the fact that the velocity gradient is very high. The PTV results clearly show the advantage of this method in near-wall regions with high velocity gradients as they provide the measurements nearest to the wall. The near-wall bias is more evident in Figure 14 which shows the difference between the measured value and true value (from the DNS data) for the mean streamwise velocity, obtained by the second PIV group and the PTV group. Figure 14a is representative of the results obtained by the first PIV group. For $y > 200$ px (about 40 WU), the agreement between the results of all contributors is very good (within ±0.02 pixels). Emphasis should be put on the very good results obtained near the wall by DLR, using a correlation method with image deformation (Willert 2004), by LIMSI using the optical flow technique, and by CORIA 2 using a PTV algorithm. Although other PIV teams also used image deformation techniques, they could not reach the same level of accuracy in this region. The other PTV teams also show a bias that is of the order of 0.5 pixels. The CORIA 2 results show a significant bias in the outer region where most of the other methods behave quite well. This should be attributed to the out-of-plane motion, which appears to be treated improperly by this algorithm (this will be confirmed by the results on the RMS velocity fluctuations described below and shown in Fig. 18). Another way to assess the accuracy on the mean value of the velocity is to plot the cumulative histogram of the velocity differences over the whole sample. This is done in Figure 15, which reveals significant differences between the different algorithms. It is interesting to note that there appear to be different groups of results that do not appear to correlate with the type of algorithm. Also, LAVIS-PTV, which shows the best performance of the PTV algorithms, is comparable to the performance of several of the advanced algorithms, but at the same time is doing much worse than the LAVIS PIV on which the predictor is based .

Figure 16 shows the profiles of the results for the streamwise turbulence intensities obtained by the first PIV group, and these are compared with the DNS data. The agreement is particularly good for this group. The results of the second PIV group show a higher level of scatter in the near wall region, but nonetheless remain within acceptable levels. It is interesting to note that several partners obtain a very good agreement on the rms (see LAVIS for example), although they show a noticeable bias on the mean value.

The wall-normal turbulence intensity is given in Figure 17 for the second PIV group. Here again, certain teams obtain results that are close to the DNS value (OSAPREF, LIMSI, DLR), but the scatter on this component is obviously larger in the outer part of the flow, where the velocity gradients are not very strong. This will be explained with the next figure. The results of the first PIV group are similar to those in Figure 17.

Figure 18 gives the profiles of the RMS error for both PIV groups and the PTV group. More significant differences appear here between the different algorithms. For PIV, above y = 100 px (about 20 WU), two groups can be distinguished: the teams using advanced algorithms having an rms error less than 0.1 pixels and those being over this value. The case of CORIA is of interest; this team used a correlation method with image deformation very similar to the one used by DLR. They used a smaller interrogation window (8×8 instead of 16×16) and obtained RMS errors significantly higher than expected on both velocity components. A check done by CORIA showed that the smoothing of the velocity field before the image interpolation in the iterative deformation process was turned off. This shows clearly the sensitivity of these advanced algorithms to the iterative procedure. Near the wall, the differences between the different teams are more important. Here again, the good results obtained by certain advanced algorithms should be emphasised. The case of LIMSI is of particular interest as they use optical flow; In contrast to the results obtained by all others, the RMS error is quite low near the wall and increases away from it. Linked to Figure 16, it seems that the optical flow technique performs quite well in regions with strong velocity gradients (similar to the results obtained by the best-performing correlation methods), but it is not so good in the outer flow region. Comparisons of instantaneous velocity maps, which are not shown here for the sake of conciseness but that are available on the Challenge web site, seem to indicate that optical flow is more sensitive to the out-of-plane loss-of-pairs. With the exception of LAVIS-PTV, the whole PTV group shows relatively larger errors compared to PIV. The particle location error is assumed to be about 0.1 to 0.2 pixels. Since the particle size is relatively small (it was optimised for PIV), the performance of the particle-image location algorithms may not be optimal. Also, for CORIA 2, a clear problem appears again in the outer flow region, which should be attributed to the out-of-plane motion that is not properly taken into account in the particle-image pairing procedure. Apart from CORIA 2, the higher RMS noise level for the PTV algorithms is not associated to a noticeable bias in the mean, as was shown in Figures 13- 15.

As far as the characterisation of turbulence is concerned, a measure of the quality of the results is given by the turbulence signal-to-noise ratio shown in Figure 19 (here only for the first PIV group). This parameter is defined as the ratio of the turbulence intensity to the RMS error. With the exception of CORIA, for which the cause of the problem has been identified, a ratio between 2 and 4 is observed on this parameter between the different algorithms. The worst results are obtained by standard algorithms (without iterative window deformation). The optical flow of LIMSI is comparable to these standard methods away from the wall; near the wall, the performance of the optical flow method improves, but cannot reach the performance of the best advanced correlation algorithms.

Another way to characterise the ability of the methods to assess the flow turbulence is to compare velocity power spectra. The results are shown in Figure 20 for the power spectra of the streamwise velocity fluctuations and for both PIV groups. The spectra are computed for a selected point near the wall, i.e. y = 32 pixels (which corresponds to about 6 wall units), as it is expected to be the most challenging case for these particular data (spectra were plotted at several distances from the wall). These spectra are compared to the corresponding DNS spectrum, computed on the same sample of instantaneous fields. As can be seen here also, significant differences appear in the ability of the different methods to resolve the small scales. Differences of more than 2 decades appear between the best and the worst results. This clearly indicates that some benefit can be gained in these regions using advanced algorithms to assess the flow turbulence, even when the differences in the mean velocity are of lesser importance (see Figures 12 and 13). The best performing algorithms are able

to bring the PIV noise down by about two orders of magnitude, corresponding to an improvement in the resolution of the small scales by a factor of 2 to 3 with respect to the standard algorithms. This PIV noise appears thus very sensitive to the applied algorithm.

The favourable results on turbulence assessment obtained by the advanced algorithms are confirmed by the probability density function of the velocity fluctuations. These were plotted extensively for the workshop. Only one sample for the DLR data is presented in Figure 21 and compared to the corresponding DNS data. The agreement is very good, and the PIV results do not show any discernible peak locking. It should be noted that this was not the case for all algorithms, where some even showed anti peak locking.

Finally, in order to assess the quality of the instantaneous data, some selected instantaneous velocity profiles were plotted and compared to the corresponding DNS data. Figure 22 gives an example of this comparison for the second PIV group. Both the instantaneous velocity and the difference to the DNS solution are plotted in this figure. As can be seen, the profile was selected in a region with particularly strong velocity gradients. Apart from locations very near to the wall, the overall agreement is fairly good. As emphasised by Figure 22b, in the outer flow region ($y > 100$ px), the results of several contributors remain within the range of ±0.2 pixels (this is also the case for the results in the first PIV group). Near the wall, discrepancies increase up to ±0.5 pixels. For several algorithms, the error is obviously correlated with the velocity gradient, but not in the same way. For PTV, Figure 23 shows a sample of particle images in the very near wall region and the instantaneous velocity vectors detected by the different teams. This figure clearly illustrates the difficulty encountered when identifying individual particle-image displacements with small particle images. All four groups are capable of qualitatively detecting the particle displacement. However, the number of detected particle images is quite different. VKI can detect a substantially larger number of particle images than the other three groups, since particle images with very small intensity differences can be detected by VKI. Also, some overlapping particle images are divided into individual particle images.

The aim of test case B was to assess the performance of the PIV and PTV algorithms on a synthetic turbulent flow with strong velocity gradients. Although synthetic images are not yet fully representative of real ones, they were selected for this test case as they allowed a precise characterisation of the statistical and spectral response of the algorithms. The images were designed to be of good PIV quality (particle image size, contrast, concentration…) and above, but not too far above, the limits of standard algorithms as far as the velocity gradients and out of plane motions are concerned. The aim was to assess the benefit brought by advanced algorithms. On this point of view, the results are clear: advanced algorithms using image deformation bring a significant advantage in region of high velocity gradient. Those using the standard correlation technique seem more robust with respect to the out-of-plane loss-of-pairs than the optical flow approach. The results obtained globally by the participants are of high quality, some of them being even of very high quality. Both the mean velocities and the turbulence quantities are properly determined. The RMS error appears to be uncorrelated with the bias error in the mean value. With respect to the results on the velocity power spectra, the advanced algorithms show a clear advantage. On the PIV side, a next step for this challenge would be to reduce the spatial resolution of the PIV images in order to push the advanced algorithms to their limit. As far as the PTV algorithms are concerned, the detection of individual particle images brings a clear improvement as compared to PIV in the near-wall region. Concerning the bias on the mean value of the velocity, by combining the

advantages of the different algorithms in the challenge, PTV can perform equally well as PIV and can obtain data in closer proximity to the wall. Concerning the RMS velocity fluctuations, the averaging procedure provided by PIV is clearly beneficial to the quality of the results. Please note that the Case B images had no added noise, and therefore the accuracy of PTV results for the actual images with a significant noise level is still in question and should be investigated in a next challenge.

6 Case C

In the past, the quantitative investigation with PIV of time dependent flow phenomena in air was a challenging task because of the technical limitations of the components. However, due to the progress in lasersand CMOS camera technology, it is nowadays easily possible to acquire PIV records digitally with frame rates of up to 2 kHz at 1k×1k pixel resolution. Thus, it seems to be likely that this promising technology will replace the well-established CCD-based PIV systems in the near future. Unfortunately, the pulse energy of diode-pumped lasers is still strongly limited at high repetition rates, and state-of-the art CMOS cameras are less sensitive and have a higher noise level compared to high-quality CCD sensors. To assess the performance and accuracy of state-of-the-art time-resolved PIV systems, a water flow experiment was installed, and the flow on the suction side of a SD7003 airfoil was investigated at 8 degree angle of attack with a Photron Fastcam APX with 2 kHz frame rate and 1/2000 second integration time (Nerger 2003). The illumination of the tracer particles was achieved with an Argon-ion laser where the intensity of the illumination was varied from left to right to study the effect of the signal-to-noise ratio on the quality of the evaluation results. The flow velocity was 0.3 m/s. Figure 24 gives an example of the recorded images. The lower right image shows the observation area and the bright line indicates the reflection of the model surface. For the investigation only the upper half of the image was selected because of the complexity of the flow near the airfoil (where a laminar separation bubble with transition and turbulent reattachment exists). For the Challenge four image pairs with different temporal separation between the illuminations were selected from this investigation. In addition to this water flow experiment, two image pairs where included in the test case that were measured in air. The illumination source was a diode-pumped laser (Pegasus from NewWave) with a 2 kHz repetition rate, and the field of view was recorded simultaneously with a PCO Sensicam and a Photron PCI. The cameras were fully aligned such that the field of view and projection of the pixel into the physical space was identical for both cameras. This test case was selected to study in particular the sensitivity and noise effects in detail. However, only the analysis of the first-mentioned water flow experiment will be discussed here.

Parameters for analysis

For the analysis all individual image pairs, each 1024×256 square-pixel in size, were pasted together with a black gap of 32 pixels in between. The composition of the image was done for three reasons. First, to keep the processing effort for the teams as small as possible. Second, to avoid that the evaluation software can be optimised for each individual sample image. Third, to study the effect of image boundaries and disturbances in the conservation of the image intensity.

For the comparison it was required to evaluate the image pair with 32×32 square-pixel interrogation windows on a regular grid (only for PIV) with 16-pixel spacing between the grid-points in both directions. The exact location of the grid-points in pixel units is:

X = 32 to 992   61 Nodes   (grid_distance_x = 16)
Y = 32 to 1664   103 Nodes   (grid_distance_y = 16)

In addition, a second evaluation was allowed with no restrictions regarding to the interrogation window size and grid-spacing; only the grid-points specified above should be part of the new grid!

Table 6 indicates for each team the size of the interrogation window and the number of iterations (more details on the algorithms are given in Table 4). Although for the optical flow methods these criteria are not well suited, the information provided by LIMSI is included in the same table for completeness. It can be seen that the number of iterations required for the evaluation of the image is quite different. To compensate the in-plane loss of pairs by using window shifting only two iterations are required (TSI). To adjust the window shifting with sub-pixel accuracy by using deformation techniques, at least three iterations have to be performed (URS). Up to eight iterations are required when the evaluation is performed with complex deformation techniques (DANTEC, DUTAE, LAVISION, UDN, DLR, PURDUE, IOT). In case of particle tracking, the number of iterations is even higher for CORIA 2 and VKI, because both teams estimate the local particle image displacement with complex PIV evaluation approaches before they start to determine the displacement of particle image pairs by using tracking methods. It is surprising that the tracking analysis performed by LAVIS after the PIV evaluation requires only 5 iterations, while their pure PIV analysis takes 6 iterations. This inconsistency results from the fact that their so-called tracking result is a modified correlation analysis, which does not require the identification of individual particle images.

Figure 25 provides, for each team, the analysis of the lower 4 sub-images in normalised form (the increasing time separation between the acquired image pairs was compensated such that the colour table becomes identical for all cases). As the image pairs were selected symmetrically around a fixed time, all results should be identical in this representation. However, the particle tracking results, presented in the left column, indicate that the number of valid displacements depends on the displacement (compare images from each team) and on the applied tracking approach (compare different teams). In addition, it becomes visible that the performance of the algorithms implemented by CORIA 2 and VKI decreases from right to left. As the magnitude of the displacement is fully compensated, this result is correlated with the low signal intensity of the particle images in this region. This problem is not observed in the results provided by OSAK, but here the number of obviously incorrect measurements is much higher (see high frequencies in the vector field). Thus it can be concluded that the number of valid measurements can be increased when for example the detection criteria is less conservative, but then the number of incorrect measurements increases when the signal-to-noise ratio is not sufficiently high. The other three columns reveal the results evaluated with pure PIV analysis methods (the evaluation performed by LIMSI is not shown because the image could be not evaluated due to the black gap between the images, where the assumption that the image intensity is conserved is not valid!). Generally, the results look quite good over the full image, i.e. independent of the magnitude of the displacement, the gradients and the variations in the particle image intensity and background noise as all evaluation methods are optimised to compensate these problems. However, a detailed look indicates the different noise

levels between the teams and the variation of the noise level for each team with increasing particle-image separation (c.f. the individual sub-images for each team). The results provided by DUTAE, PURDUE, UDN are quite smooth, in comparison to the results of the other teams. DLR, FOI, OSAPREF and URS show very little smoothing effects, and DANTEC, IOT, LAVISION, TSI, URS2 show nearly none. As the size of the interrogation windows was identical (see table 6) this smoothing is obviously associated with the determination of the transformation parameter for the window deformation approach from the global vector field. In effect, it can be concluded that the spatial resolution is artificially decreased. To study this effect in detail, images with high spatial frequencies need to be analysed in detail. Another interesting problem is the accumulation of spurious vectors at the left border of some vector fields (for example, see the TSI results). This effect is typical of second order window-shifting methods and methods based on differently-sized interrogation windows, because one sample window does not fully overlap with the image. Teams who do not show these effects must have implemented special features in their algorithms to avoid this effect, but undoubtedly the quality of the result is usually reduced at the image boundaries because of the loss of information. The consistency of the evaluation approach for each individual team can be deduced from the analysis of the four sub-images, because the relative measurement error decreases from top to bottom due to the increasing temporal separation between the image pairs. Thus, the lower image for each team can be seen as a true solution, as the measurement error is reduced by a factor of four relative to the upper sub-image of the sequence. For this reason the smoothness increases from top to bottom.

To make the effect of peak-locking evident, the histogram was calculated for each team as shown in Figure 26. In addition, the average and standard deviation were computed over all results listed in the legend, in order to quantify the quality of the results. Theoretically the average graphs for the different fields should be nearly equal as the flow and the acquisition parameters are identical, but due to the increased dynamic range from top to bottom (up to a displacement of 20 pixels for field1, according to figure 26, and only maximum displacement of 5 pixels for field4!) the detailed structure of the displacement field becomes visible. However, due to the large particle-image sizes, which are typical for applications in water, the results in general do not show significant peak locking, but the deviations of some teams from the average result should be noted (see for example OSAPREF, FOI and UDN).

To compare the results locally, the normalised displacement $\Delta x'$ along the y axis at x = 512 px is shown in Figure 27 for the upper (left) and bottom (right) displacement fields. This particular x position was selected for two reasons: First, because here curvature effects can be neglected, as the flow is nearly straight. Second, the signal-to-noise ratio for this position is quite good for all teams. The comparison between the two results allows a direct estimation of the measurement error for each team and of the consistency of the analysis method. It can be concluded from this analysis that the measurement error is below 0.1 pixel on average.

To assess for each team the relative measurement error quantitatively, the result with the lowest measurement error (i.e., field1) was normalised and afterwards subtracted point-wise from field4 (only at locations with valid vectors in both fields) to determine the average of the remaining difference expressed in pixel units and as a percentage. Table 7 shows this error for the horizontal displacement component. First of all, it can be concluded that the measurement error is surprisingly good for many teams. When the displacement in the x direction is considered, the average error due to the evaluation is only around 0.09 pixels, or 2.3%, for this particular test case! The best result

was provided by UDN with an error of 1.28%, followed by IOT, DLR, LAVISION, PURDUE, DUTAE, FOI/FFA, URS, DANTEC, OSAPREF, LIMSI, URS2 and TSI Thus, the best result provided by UDN is 3.8 times better compared to the TSI result. This is well within an order of magnitude, but the differences indicate nicely what can be gained by using sophisticated analysis methods.

7 Conclusion

The contents of this paper describes the results of the second PIV challenge, held in 2003. The test cases were selected taking into account the lessons of the first Challenge in 2001, and with a stronger focus on the assessment of turbulence. As in the first Challenge, the participation was numerous and of high level. One could regret that the participation on PTV was smaller this time. Obviously, the major contribution was from Europe. All the contributors are gratefully acknowledged for their efforts and good work they performed.

A general remark, as compared to the first Challenge, is that the fact of providing series of images has made it possible to carry out a statistical analysis of the results, which was more fruitful quantitatively than the analysis performed on single-image sets in the first Challenge.

For case A the overall agreement of the data for the axial displacements are quite good, and the differences in the profiles for the turbulence intensity in the outer flow region and in the fractional displacement histograms (i.e., 'peak locking') could generally be understood in terms of the known performance of PIV interrogation and sub-pixel interpolation. However, there are some remarkable differences in the results for the radial displacements. First of all, it is noteworthy that the largest differences occur in the region where there is no turbulence; in this flow region the displacement is nearly uniform with a magnitude that is well below 1 pixel. This corresponds to the analysis of uniformly translated test objects, but in the present case it turns out to be a challenge to measure this aspect of the flow. The radial velocity in the outer jet region, or entrainment velocity, is closely related to the jet spreading rate (i.e., the jet mass increases as non-turbulent fluid becomes entrained by the turbulent jet). The fact that the observed entrainment velocities from the PIV and PTV data are significantly under-estimated or over-estimated implies that the PIV and PTV results—in a strict sense—do not comply with the conservation of mass. It seems that there is still room for improvement for PIV interrogation algorithms. Also, we would like to note that for case A there does not seem to be a significant difference in PIV interrogation performance between the 'standard' PIV interrogation algorithm (using multi-pass interrogation with discrete-offset window shifting and 3-point Gaussian sub-pixel interpolation) and 'advanced' PIV interrogation algorithms, like image deformation and 'optical flow' methods. As for the PTV results, it should be noted that the original experiment was optimized for PIV analysis; it is therefore an even greater challenge for a PTV analysis, and quite remarkable that the PTV algorithms perform quite well with images that are obviously not optimal for PTV analysis. Therefore, no further conclusions with respect to the PTV performance seem appropriate at this point.

As far as case B is concerned, a quite detailed statistical characterisation could be performed by comparison with the DNS data. Globally, it appears that the mean velocity is fairly well predicted by all the algorithms. The bias is of the order of ± 0.02 pixels in most of the field, and reaches ± 0.3 pixels at the points closest to the wall for certain teams. Differences between the algorithms are clearly evident on this point of view by the cumulative histograms of the measurement error for the

velocity. For the turbulence intensities , a clear advantage is shown by advanced algorithms using multi-grid, multi-pass and window (or image) deformation. This is particularly true in regions of strong velocity gradients. Interestingly, the optical flow technique used by LIMSI is doing very well in regions of strong velocity gradient, but seems more sensitive to out-of-plane loss-of-correlation than the best-performing correlation methods (some correlation methods show the same sensitivity to out-of-plane motions). Another clear point is that advanced algorithms are quite sensitive to the implementation and programming strategy. The results obtained on the turbulence spectrum are also very demonstrative of the fact that a lot can be gained on the assessment of turbulence by the use of ingenious algorithms. These results also clearly demonstrate that the PIV noise has the same characteristics as white noise, as the mean velocity results does not seem to be affected strongly by the strong differences in noise level observed between the different contributors on the spectral data.

The PTV approach has a clear advantage for the measurement in the very near wall region, since the displacement of individual particle images can be measured. However, the RMS error is relatively large because of the particle location error. This particle location error should be reduced to improve the accuracy. The present test case was performed with noise-free synthetic images. Actual images, which generally incorporate a significant noise level, may have an unfavourable effect on the performance of PTV algorithms. This point should be investigated further in a next challenge.

Regarding case C, apart from the accumulation of spurious vectors at the left border of some vector fields the results are quite good and independent of the magnitude of the displacement, the gradients and the variations in particle image intensity and background noise. A detailed inspection of the results shows again the different noise levels reached by the different teams and the variation of the noise levels for each team with increasing particle image separation. Due to the large particle-image sizes, which are typical for applications in water, the results in general do not show serious peak locking. The average error due to the evaluation is around 0.09 pixel for this particular experimental test case! The best result was provided by UDN with an error of 0.05 pixel. The improvement brought by the state-of-the-art methods is clearly visible on this test case.

Globally, most of the state-of-the-art methods were present and most of the commercially-available PIV methods too. The global agreement between the different methods is quite good, but the differences that appear in some specific regions of the flow are significant and show that certain algorithms perform better than others in the same regions. In particular, the noise level provided by the different algorithms is significantly different. Also, the advantage of the "advanced algorithms", is clear on the synthetic images of case B in the region of strong gradient and in case C. It is not so obvious on the real images of case A. Unfortunately there is not a single algorithm that has the best performance everywhere. As a difference to the previous Challenge, the discrepancies observed here could be used as a guide for the improvement of the algorithms.

An important conclusion is that synthetic images are not yet fully representative of real images, as the agreement is much better in case B than in Case A. An effort to generate more representative synthetic images is necessary. Besides, the advanced algorithms using window deformation allow for the assessment of stronger velocity gradients, and Case B could have been more demanding on the PIV algorithms. Finally, the influence of the out-of-plane component should be studied in more detail.

The conclusion of the workshop was that it is worth preparing a third Challenge, with test cases that allow a more advanced analysis of the spatial resolution of the algorithms and with the inclusion of stereoscopic PIV data in order to evaluate the different reconstruction techniques. This Challenge will start at the end of 2004 and will be concluded by a workshop on September 2005, linked to the PIV'05 symposium at Caltech in Pasadena (USA).

Acknowledgement

References

Cardone G.; Nese F. G.; Astarita T.; Carlomagno G. M. (2002) Experimental investigation of a round jet in cross-flow. 10th International Symposium on Flow Visualization, Kyoto, Japan.

Di Florio D.; Di Felice F.; Romano (2002) G. P. Windowing, re-shaping and re-orientation interrogation windows in particle image velocimetry for the investigation of shear flows.Meas. Sci. Technol. 13 pp 953–962.

Foucaut J.M., Miliat B., Perenne N., Stanislas M. (2004) Characterization of different PIV algorithms using the EUROPIV Synthetic Image Generator and real images from a turbulent boundary layer. Proceedings of the EUROPIV 2 workshop held in Zaragoza, - Spain, March 31– April 1, 2003 - Stanislas, M. Westerweel, J. and Kompenhans, J., Springer - ISBN 3-540-21423-2.

Fukushima, C., Aanen, L. & Westerweel, J. (2002) 'Investigation of the mixing process in an axisymmetric turbulent jet using PIV and LIF.' In: *Laser Techniques for Fluid Mechanics* (Eds. R.J. Adrian *et al.*) Springer:Berlin, pp. 339-356.

Keane R.D., Adrian R.J., (1990), Optimisation of particle image velocimeters – Part I : Double pulsed systems Measurement Science and Technology, vol.1, pp 1202-1215.

Keane R.D., Adrian R.J., (1992), Theory of cross-correlation analysis of PIV images, Applied Scientific Research, vol 49, pp 191-215.

Lecordier B., Trinité M. (2004) Advanced PIV algorithms with image distortion for velocity measurements in turbent flows - Proceedings of the EUROPIV 2 workshop held in Zaragoza, - Spain, March 31– April 1, 2003 - Stanislas, M. Westerweel, J. and Kompenhans, J., Springer - ISBN 3-540-21423-2.

Nerger D, Kähler CJ, Radespiel R: Zeitaufgelöste PIV Messungen an einem schwingenden SD7003-Profil bei Re=6×10^4. Lasermethoden in der Strömungsmesstechnik, 10. Fachtagung der Deutschen Gesellschaft für Laser-Anemometrie GALA e.V., Braunschweig, 2003.

Ohmi K.; Hang Yu L. (2000) Particle tracking velocity with new algorithms. Meas. Science & Technol. 11, pp 603-616.

Okamoto, K., Nishio, S., Kobayashi, T., Saga, T., Takehara, K., (2000a), "Evaluation of the 3D-PIV Standard Images (PIV-STD Project)," J. Visualization, 3-2, 115-124.

Okamoto, K., Nishio, S., Saga, T. and Kobayashi, T., (2000b), "Standard images for particle-image velocimetry," Meas. Sci. Technol., 11, 685-691.

Quénot G.M.; Pakleza J.; Kowalewski T.A. (1998) Particle Image Velocimetry with Optical Flow. Exp. in Fluids, vol 25-3, pp 177-189.

Rajaratnam, N. (1976) *Turbulent Jets.* Elsevier:Amsterdam.

Scarano F.; Riethmuller M. (2000) Advances in Iterative multigrid PIV image processing. Exp. Fluids Supplement 29, S51-S60.

Scarano F. (2002) Iterative image deformation methods in PIV. Meas. Sci. Technol. 13 R1–R19

Stanislas M.; Okamoto K.; Kaehler C. (2003a) Main results of the first international PIV Challenge. Measurement Science & Technology **14**, R63-R89.

Stitou A.; Riethmuller M.L. (2001) Extension of PIV to Super Resolution using PTV. Measurement Science and Technology, Vol 12, Nr 9, pp 1398-1403.

Sugii Y., Nishio S., Okuno T., Okamoto K. (2000) A highly accurate iterative PIV technique using gradient method. Measurement Science and Technology, Vol.11, pp 1666-1673.

Susset A.; Most J. M.; Honoré D. (2003) A novel architecture of super-resolution PIV algorithm for the improvement of large velocity gradient resolution. 5th International Symposium on Particle Image Velocimetry Busan, Korea.

Wereley S.T. ; Gui L.C. (2002) Advanced algorithms for microscale Particle Image Velocimetry. AIAA Journal vol 40 n°6.

Westerweel J. (2000a) 'Theoretical analysis of the measurement precision in particle image velocimetry.' *Exp. Fluids* **29** S3-12.

Westerweel J. (2000b) 'Effect of sensor geometry on the performance of PIV interrogation.' In: Laser Techniques Applied to Fluid Mechanics (Eds. R.J. Adrian et al.), Springer-Verlag:Berlin. pp. 37-55.

Westerweel J. (1997) 'Fundamentals of digital particle image velocimetry.' Meas. Sci. Technol. 8: 1379-1392.

Westerweel J., D. Dabiri & M. Gharib (1997) 'The effect of a discrete window offset on the accuracy of cross-correlation analysis of digital PIV recordings.' Exp. Fluids 23: 20-28.

Westerweel J., A.A. Draad, J.G.Th. van der Hoeven & J. van Oord (1996) 'Measurement of fully-developed turbulent pipe flow with digital particle image velocimetry.' Exp. Fluids 20: 165-177.

Willert C. (2004) Application potential of advanced PIV algorithms for industrial applications. Pivnet/ERCOFTAC workshop on Particle Image Velocimetry, Lisbon, July 9-10.

Version 8 january 11th 2004

Table 1 Scientific committee of the first PIV Challenge

Name	Country	address
Pr T. Kobayashi	Japan	Institute of Industrial Science University of Tokyo (Japan)
Pr Nishio	Japan	Kobe Univity of Mercantile Marine (Japan)
Pr K. Okamoto	Japan	University of Tokyo Nuclear Eng. Res. Lab. (Japan)
Pr R.J. Adrian	USA	University of Illinois at Urbana Champaign, Theoretical and Applied Mechanics Laboratory (USA)
Dr C. Kähler	Europe	Technical University Braunschweig (Germany)
PR J. Westerweel	Europe	Delft University of Technology, Laboratory for Aero & Hydrodynamics (The Netherlands)
Pr M. Stanislas	Europe	Laboratoire de Mécanique de Lille France

Table 2 Test cases of the second PIV Challenge

Case n°	Description	Provider	Image type	Number of sets
A	Axisymetric turbulent jet in stagnant surrounding	Westerweel	real	100
B	Turbulent channel flow from DNS	Okamoto	synthetic	100
C	Patchwork of different CCD cameras.	Kähler	real	1

Version 8 january 11th 2004

Table 3 List of contributors

Team acronym	Company & address	Contact name	PIV PTV
FOI	FOI Bromma (Sweden)	A. Svard	PIV
DUTAE	Delft Univ. of Tech. Aero. Eng. (Netherlands)	F. Scarano	PIV
PURDUE	Purdue Univ. Mech. Eng. West Lafayette, IN and University of Mississippi, Oxford, MS (USA)	S. Wereley L. Gui	PIV
CORIA 1	CORIA UMR CNRS 6614 Rouen (France)	B. Lecordier	PIV
CORIA 2	CORIA UMR CNRS 6614 Rouen (France)	A. Susset	PTV
URS	University of Rome La Sapienza (Italy) - INSEAN	G.P. Romano F. Di Felice	PIV
LAVIS	Lavision GmbH Göttingen (Germany)	B. Wieneke	PIV & PTV
VKI	Von Karman Institute (Belgium)	M. Riethmuller	PTV
OSAK	Osaka Sangyo University (Japan)	K. Ohmi	PTV
UDN	Universita di Napoli "Federico II" (Italy)	G. Cardone	PIV
IOT	Institute of Thermophysics, Siberian Branch of RAS (Russia)	D. M. Markovich	PIV
DANTEC	Dantec Dynamics A/S (Sweden)	B. Beltoft Madsen	PIV
DLR	Institute of Propulsion Technology German Aerospace Center (Germany)	Chris Willert	PIV
OSAPREF	Osaka Prefecture University (Japan)	Taki Okuno	PIV
LIMSI	LIMSI-CNRS UPR (France)	F Lusseyran	PIV
TSI	TSI France Inc. (USA)	J. Stefanini,	PIV

Table 4a Parameters used by the contributors for PIV processing

Team acronym	Method	Algorithm	iter	IW size	Filter size	Grid size	Init. grid size	Peak detection
FOI	CCF	MP MG	0	32x32	0x0	16x16	64x64	3P Gaussian
DUTAE	CCF 2nd order	MP MG AWD	8	37x37	37x37	8x8	200x200	3P Gaussian
PURDUE	CCF	MP MG AWD	5	32x32	0x0	16x16	0x0	3P Gaussian
CORIA 1	CCF	MP MG AWD	3	16x16	0x0	4x4	0x0	2D Gaussian 3x3
URS	CCF	MP AWS	3	32x32	32x32	16x16	128x128	3P Gaussian
LAVIS	CCF	MP MG AWD	5	32x32	16x16	8x8	32x32	3P Gaussian
UDN	CCF	MP MG AWD	7	16x16		8x8	64x64	9P Gaussian
IOT	CCF	MP MG AWS	2	32x32	32x32	16x16	32x32	3P Gaussian
DANTEC	CCF	MP AWD	8	20x20	20x20	16x16	32x32	2D Gausian 3x3
DLR	CCF	MP MG AWD	4	16x16	16x16	8x8	64x64	2D Gaussian LM 7x7
OSAPREF	CCF	MP AWS	3	16x16	8x8	8x8	16x16	Gradient
LIMSI	Opt Flow	MP ASD	28	7x7	5x5	1x1	358x358	DP max
TSI	CCF	MP AWS	2	32x32	32x32	16x16	64x64	3P bilinear

MP : multi pass, MG : multi grid, AWD : adaptive window deformation, ASD : adaptive strip deformation, DP max : dynamic programming, maximum subpixel, AWS : adaptive window shifting.

Table 4b : Parameters used by the contributors for PTV processing

Team acronym	Method	CC Algorithm	Particle detection and pre-processing	Tracking criteria
CORIA2	CCF	MP MG AWD	Threshold and median filter	Displacement
LAVIS-ptv	CCF	MP MG AWD	Threshold and low-pass filtering	Displacement
OSAK	relaxation	-	Dynamic threshold and low-pass filtering	Displacement and angle
VKI	Hybrid piv-ptv	MG AWD	Threshold and peak finding	Displacement

Version 8 january 11th 2004

Table 5 Parameters for the analysis of Case A.

team	equid.	resol.	method	nr. vect.	discarded	outl.	perc.	pk. lock.	A	B	entr. vel.
CORIA 1	yes	16×16	CCF	6076000	8449	957	0.15%	0.0016	-6085	0.1312	-0.113
CORIA 2	no		hybr. PIV/PTV	2426441	not lab.	6272	0.26%	0.0144	-6387	0.1315	-0.066
DANTEC	yes	24×24	CCF	372100	18450	7	4.96%	0.0030	-5937	0.1338	-0.105
DLR	yes	20×20	CCF	1525200	641	665	0.09%	0.0012	-6148	0.1301	-0.111
DUTAE	yes	31×31	CCF/2nd ord.	1452000	0	280	0.02%	0.0014	-6042	0.1327	-0.155
FOI	no	32×32	opt. flow	372000	6939	173	1.91%	0.0054	-5870	0.1358	-0.111
IOT	yes	32×32	CCF	372100	119	109	0.06%	0.0029	-6197	0.1284	-0.093
LAVIS	yes	32×32	CCF	1550000	509	262	0.05%	0.0013	-6163	0.1296	-0.079
LAVIS PTV	no		hybr. PIV/PTV	5102843	0	3023	0.06%	0.0008	-6240	0.1277	-0.155
LIMSI	yes	12×12	opt. flow	1550000	0	362	0.02%	0.0020	-6041	0.1319	-0.076
OSAK	no	64×64	PTV	1297007	not lab.	172229	13.28%	0.0619	-3661	0.1703	-0.140
OSAPREF	yes	?	CCF	1525200	57493	528	3.80%	0.0176	-6250	0.1282	-0.062
PURDUE	yes	32×32	CCF	390600	22	67	0.02%	0.0007	-6085	0.1315	-0.144
TSI	yes	32×32	CCF	372100	7334	4	1.97%	0.0032	-6002	0.1317	-0.090
UDN	yes	32×32	CCF	372100	26974	8	7.25%	0.0014	-6179	0.1288	-0.119
URS	yes	32×32	CCF	366000	90394	20	24.70%	0.0071	-6026	0.1327	-0.120
VKI	no		hybr. PIV/PTV	917735	not lab.	166	0.02%	0.0159	-5858	0.1366	-0.100

equid. = equidistant grid; resol. = size of interrogation domain; method: CCF = cross-correlation function; nr. vect. = number of vectors; discarded = number of vectors labelled as discarded; outl. = number of vectors outside displacement range; perc. = fraction of discarded vectors and outliers; pk. lock. = 'peak locking' coefficient; A = coefficient for the centreline velocity (in px^2); B = jet spreading rate; entr. vel. = entrainment velocity for $800<x<950$, $850<y<900$.

Table 6 Parameters used by the contributors for case C.

Method	Team	ev_size	ev_iter
PIV	FOI/FFA		
PIV	DUTAE	31 x 31	8
PIV	PURDUE	32 x 32	5
PIV	URS	32 x 32	3
PIV	URS2	16 x 16	3
PIV	LAVIS	32 x 32	7
PIV	UDN	32 x 32	7
PIV	IOT	32 x 32	4
PIV	DANTEC	32 x 32	8
PIV	DLR	32 x 32	5
PIV	OSAPREF		
PIV	LIMSI	12 x 12	30
PIV	TSI	32 x 32	2
PTV	CORIA 2	70 x 30	12
PTV	VKI	16 x 16	12
PTV	OSAK		
PTV	LAVIS_PTV	32 x 32	6

Table 7 Relative measurement error on case C.

number	Team	dx [px]	dx [%]
1	UDN	0.0489	1.2750
2	IOT	0.0606	1.5808
3	DLR	0.0618	1.6201
4	LAVISION	0.0653	1.7035
5	PURDUE	0.0707	1.8429
6	DUTAE	0.0714	1.8581
7	FOI/FFA	0.0845	2.2118
8	URS	0.0882	2.3046
9	DANTEC	0.0890	2.3233
10	OSAPREF	0.0896	2.3597
11	LIMSI	0.1024	2.5764
12	URS2	0.1192	3.1143
13	TSI	0.1811	4.8716
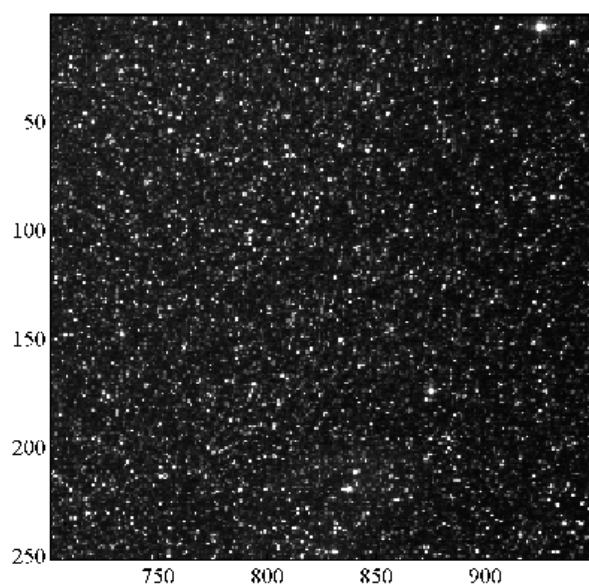
Figure 1 A 256×256-pixel detail from the top-right corner of the 992×1004-pixel image 'fj001a.tif'.
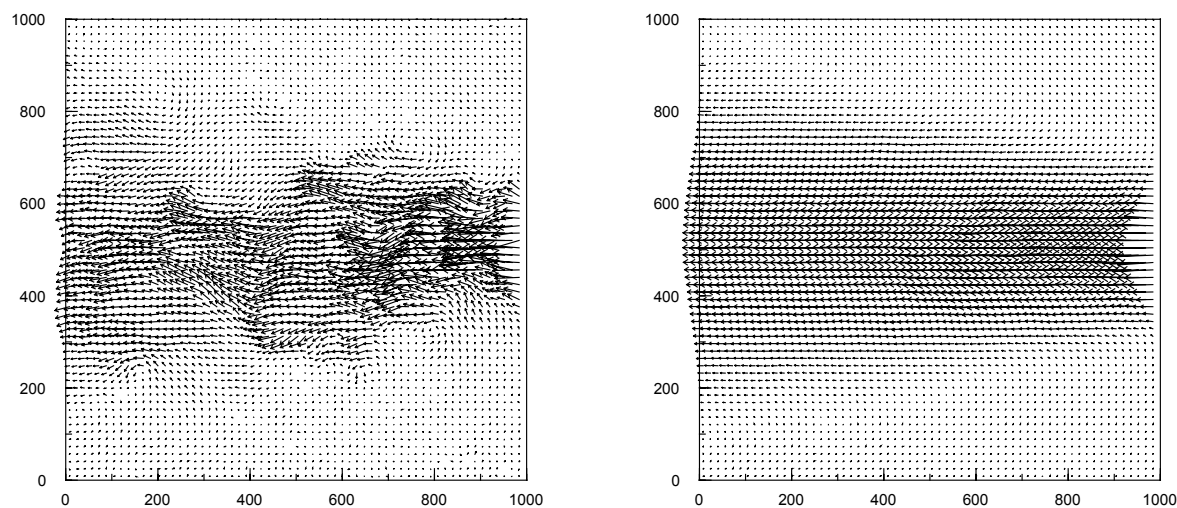
Figure 2 Instantaneous (left) and mean (right) displacement field for Case A (at 32×32-pixel interrogation resolution).
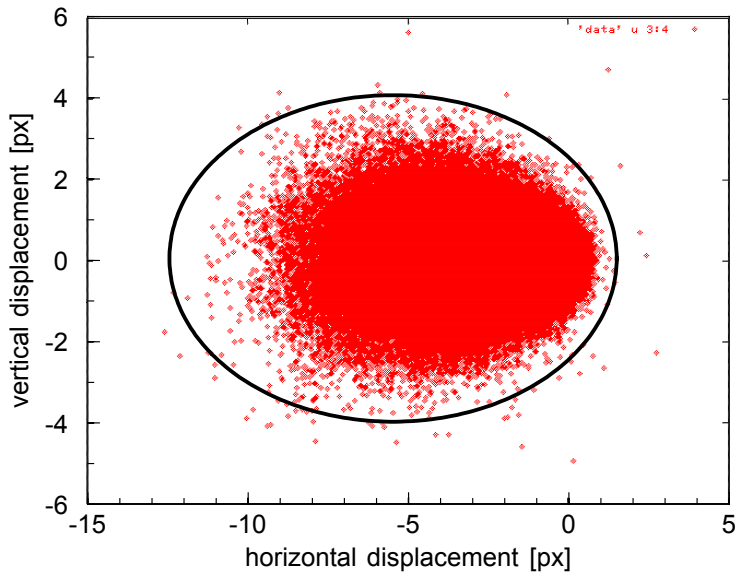
Figure 3 Scatter plot of the measured displacements for Case A. All data outside the ellipse are considered to be outliers.
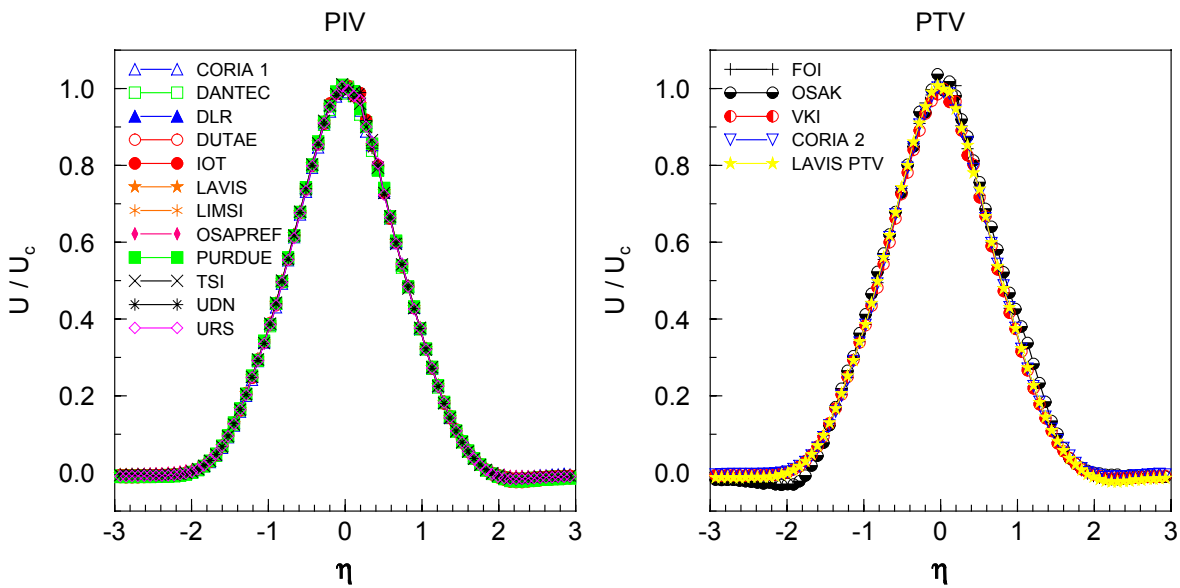
Figure 4 The scaled results for the mean axial velocity as a function of the reduced radial coordinate $\eta = (y - y_0) / \ell(x)$ for the PIV (left) and PTV (right) analysis of Case A.
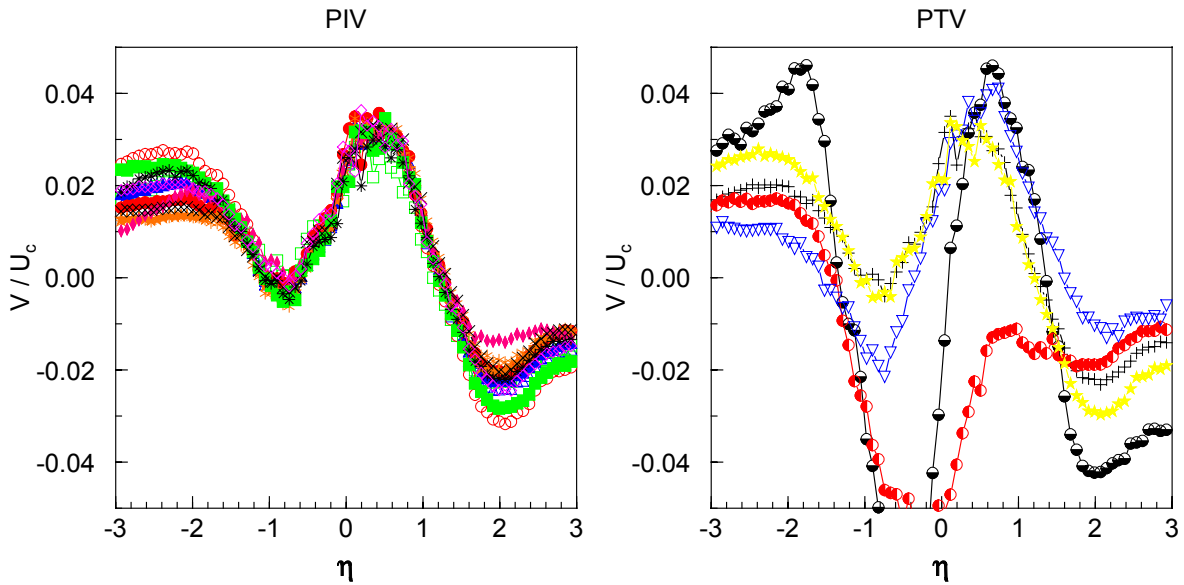
Figure 5 The scaled results for the mean radial velocity as a function of the reduced radial coordinate η for the PIV (left) and PTV (right) analysis of Case A. Symbols as in Figure 4.
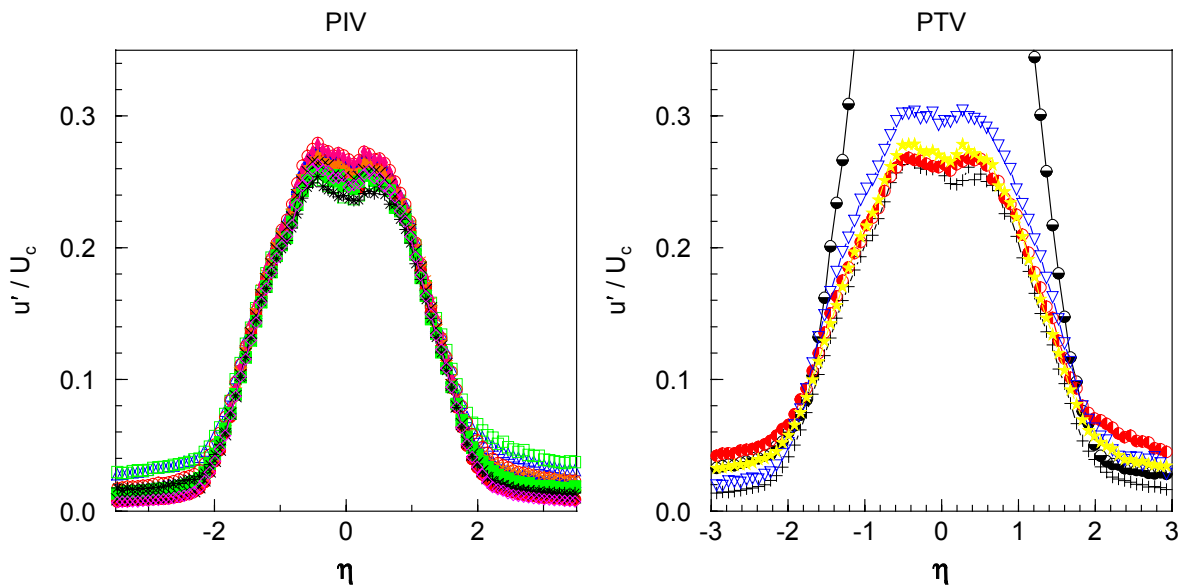
Figure 6 The scaled results for the rms axial velocity fluctuation as a function of the reduced radial coordinate η for the PIV (left) and PTV (right) analysis of Case A. Symbols as in Figure 4.
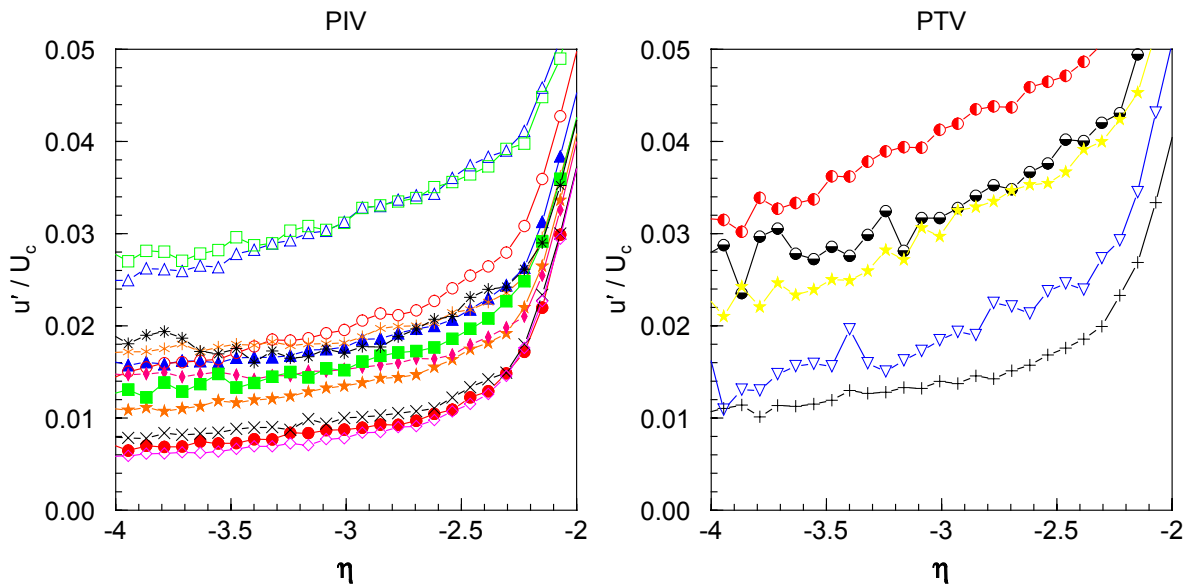
Figure 7 Detail from the graphs in Figure 6. Symbols as in Figure 4.
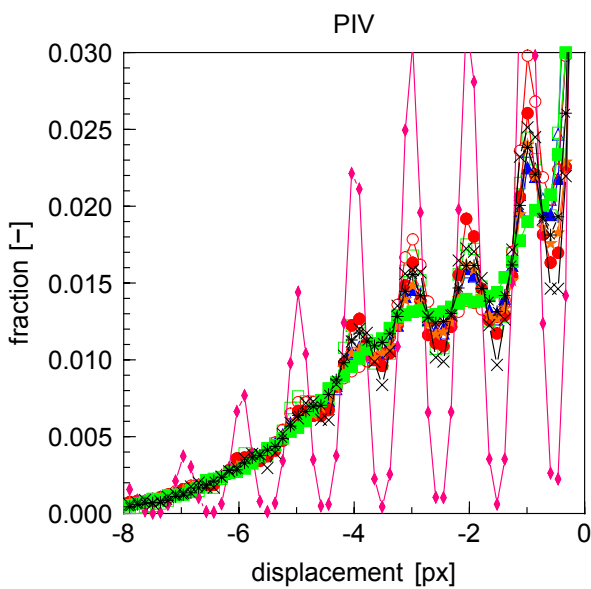
Figure 8 The histogram for the axial displacement in pixel units [px] for the PIV results of Case A. Symbols as in Figure 4.
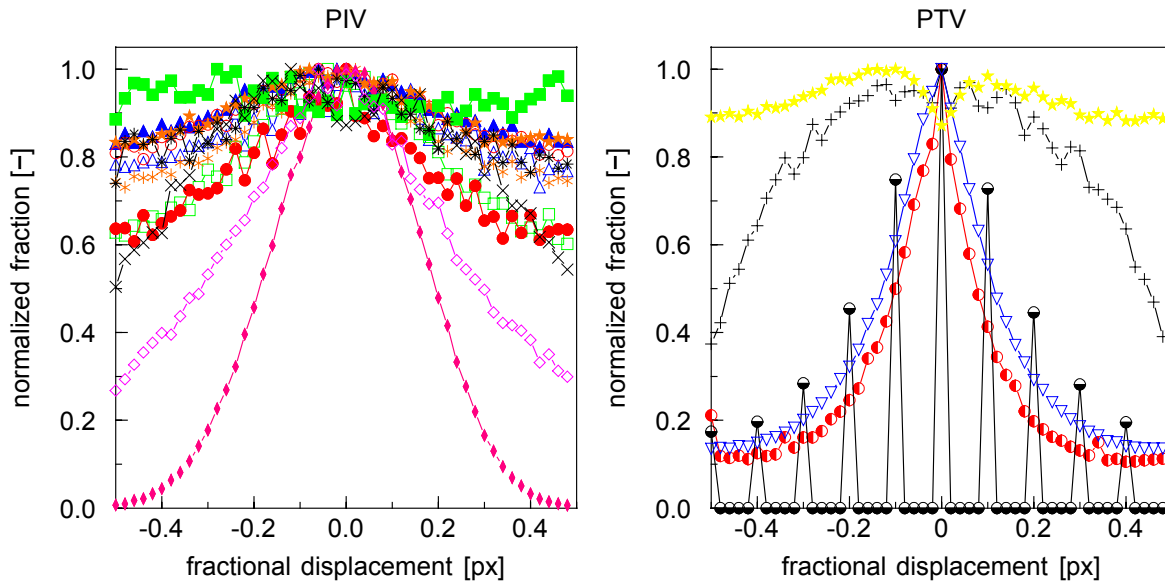
Figure 9 The histograms of the fractional displacement in pixel units [px], normalized with respect to the maximum histogram value for the PIV and PTV data of Case A. Symbols as in Figure 4.
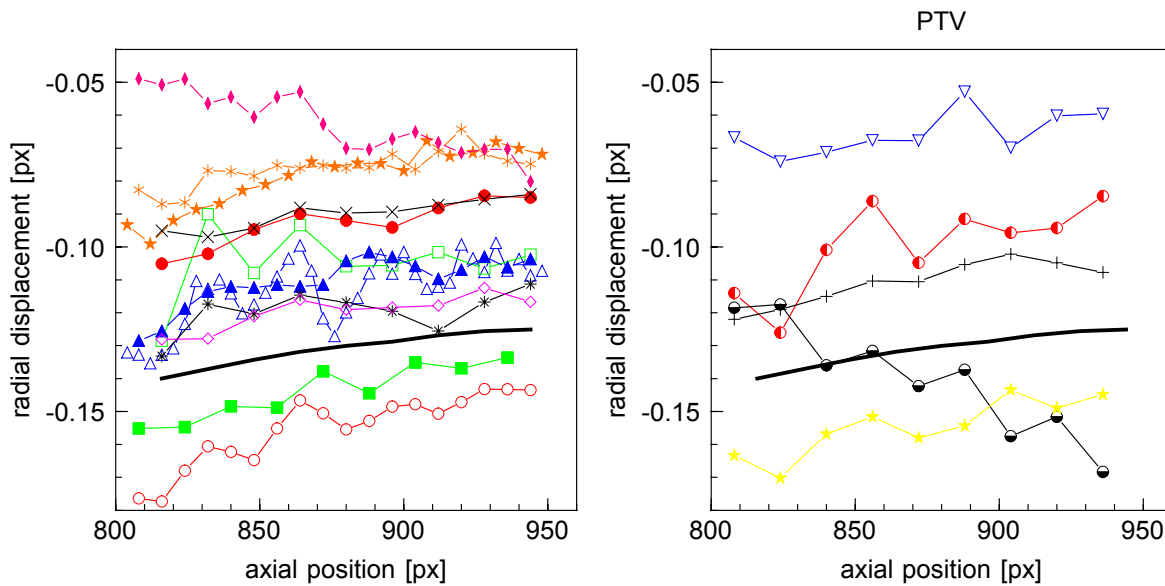
Figure 10 The mean radial displacement in pixel units [px] (proportional to the entrainment velocity) as a function of the axial position (in [px]) for the PIV and PTV data of Case A. The solid line represents the measured value using a larger time delay (see text). Symbols as in Figure 4.
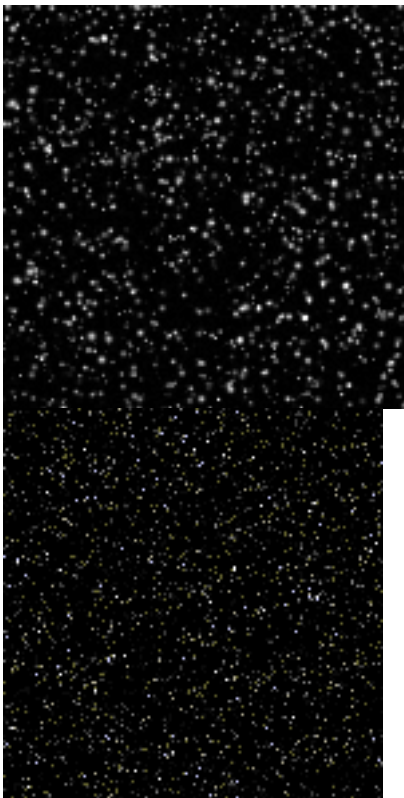
Figure 11 Piece of a sample image from case B
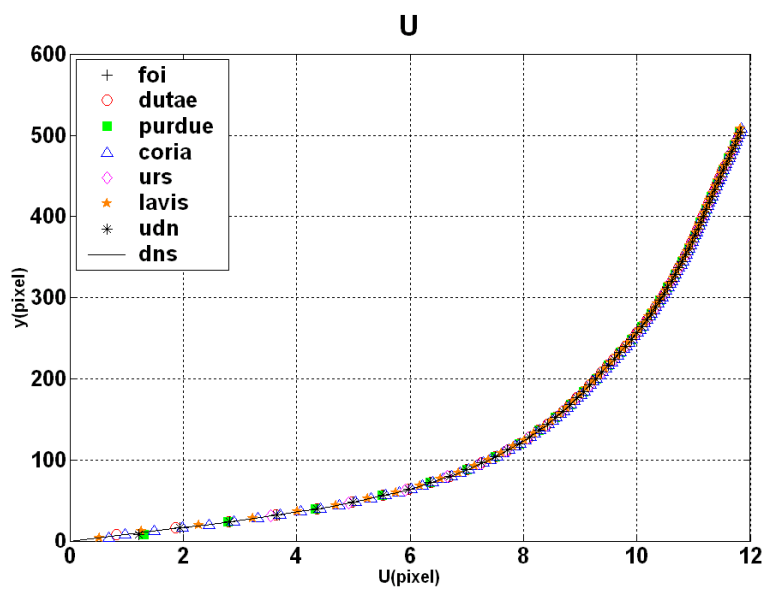
Figure 12 Mean velocity profile obtained by the first PIV group, compared to the DNS

a)

b)

c)
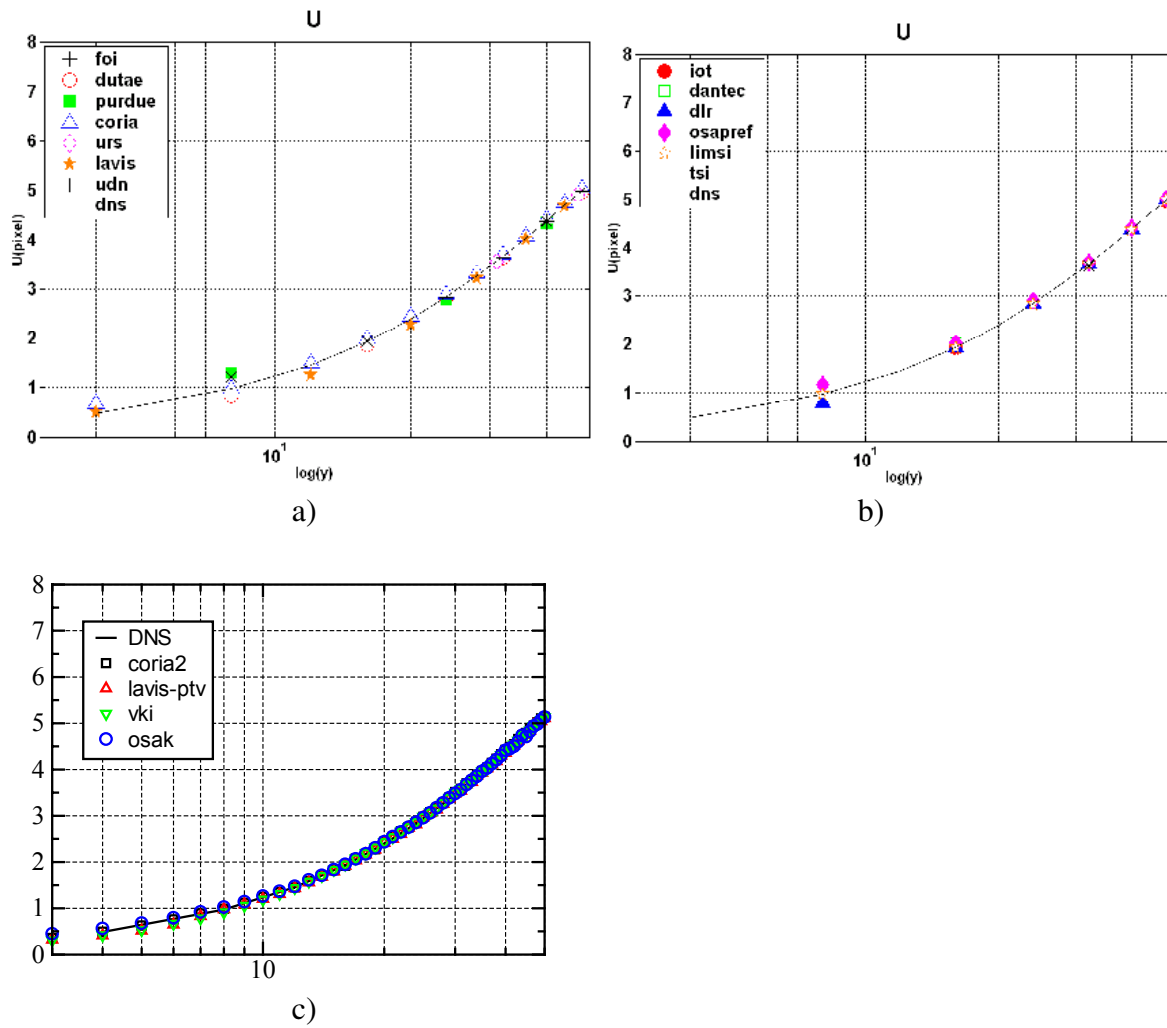
Figure 13 Mean velocity profile obtained by a) the first and b) the second PIV group and c) the PTV group, enlargement of the near wall region.

a)

b)
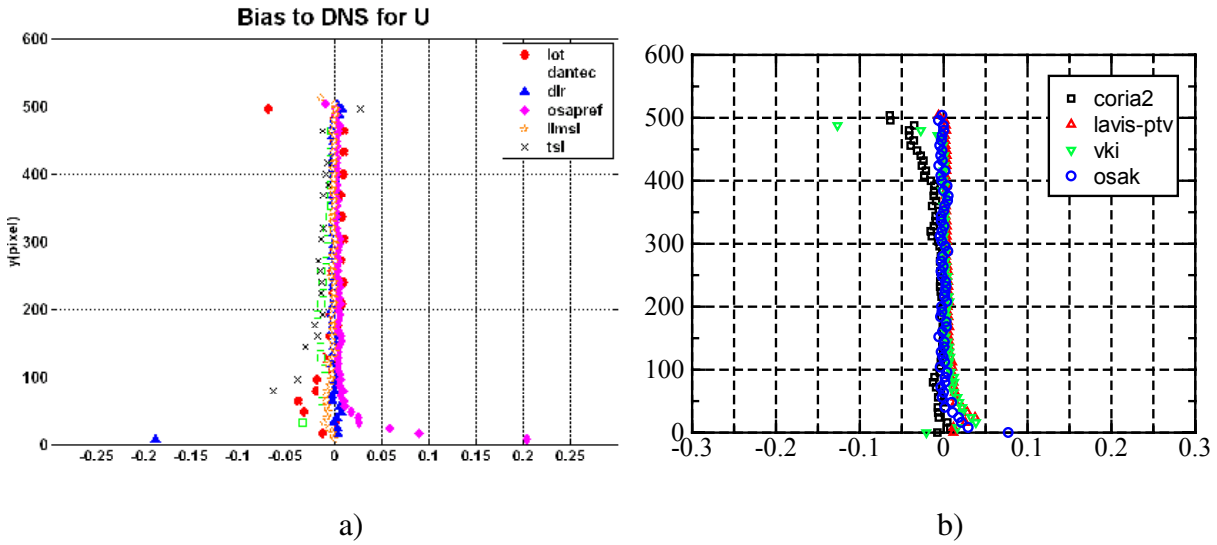
Figure 14 Bias to the DNS mean velocity obtained by a) the second PIV group and b) the PTV group.

a)

b)

c)
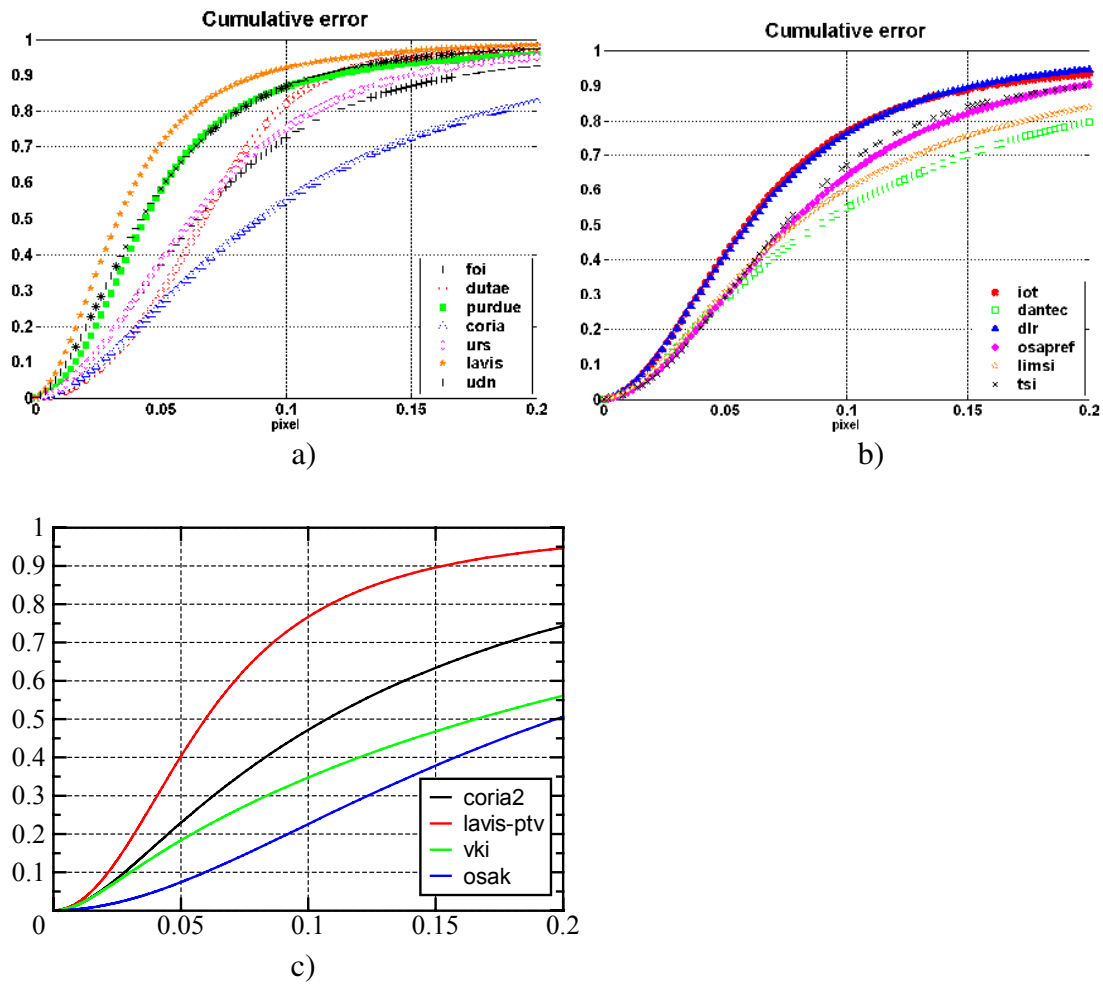
Figure 15 Cumulative histogram of the error on the velocity obtained by a) the first and b) the second PIV group and c) the PTV group.
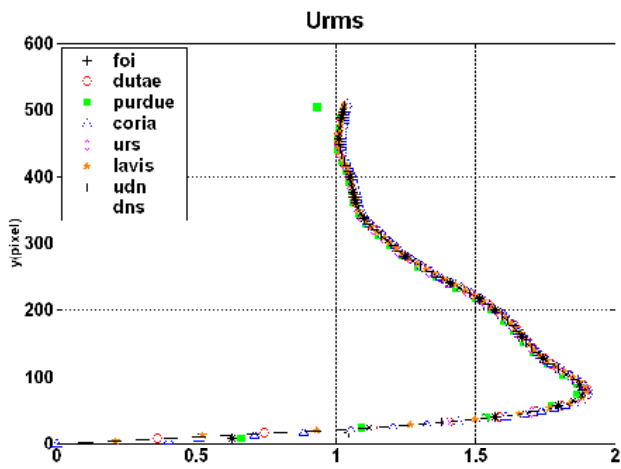
Figure 16 Streamwise turbulence intensity obtained by the first PIV group compared to the DNS.
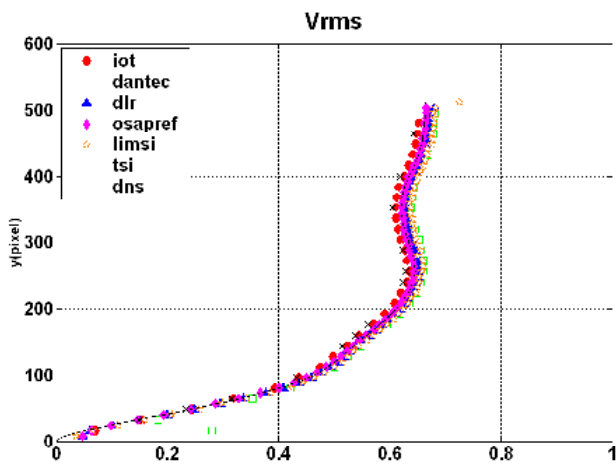
Figure 17 Wall normal turbulence intensity obtained by the second PIV group compared to DNS.
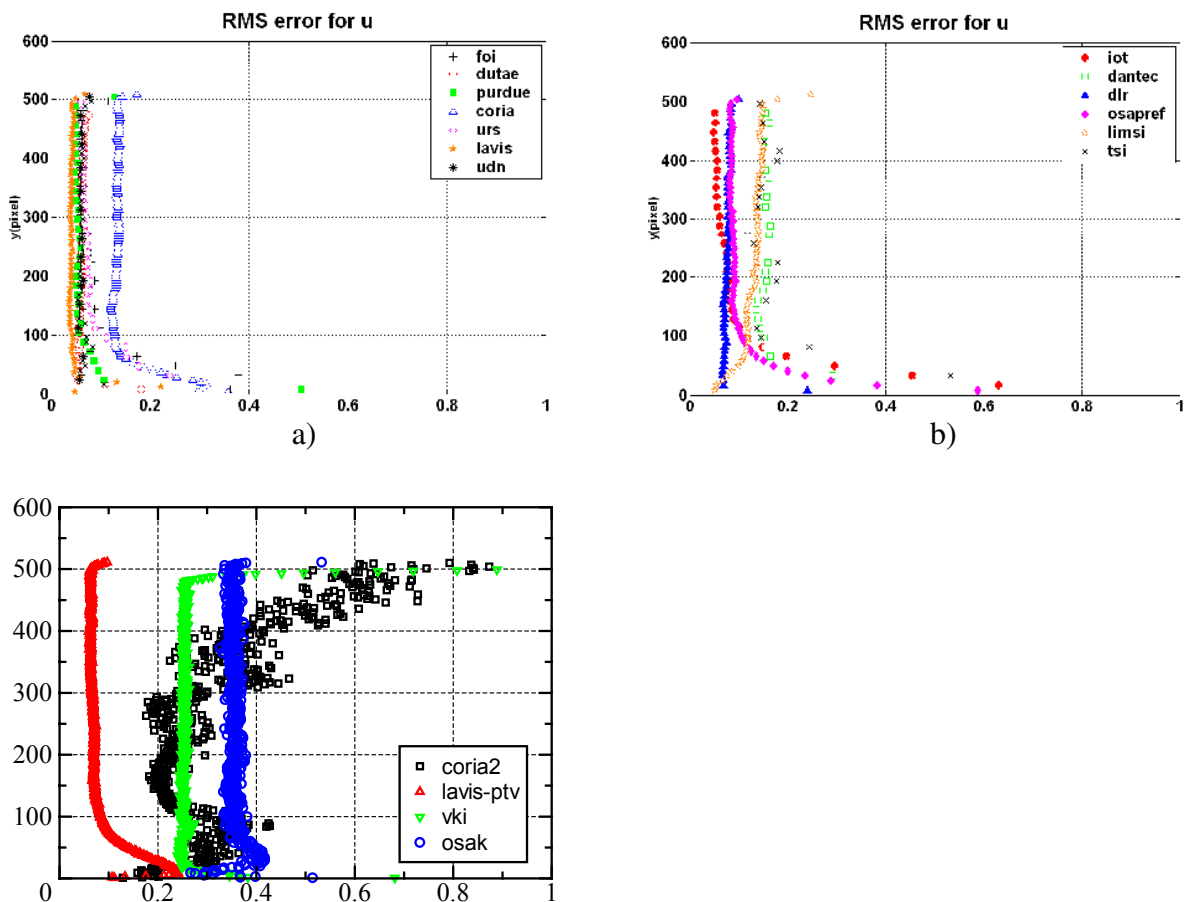
Figure 18 RMS error on the streamwise velocity component obtained by a) the first and b) the second PIV group and c) the PTV group.
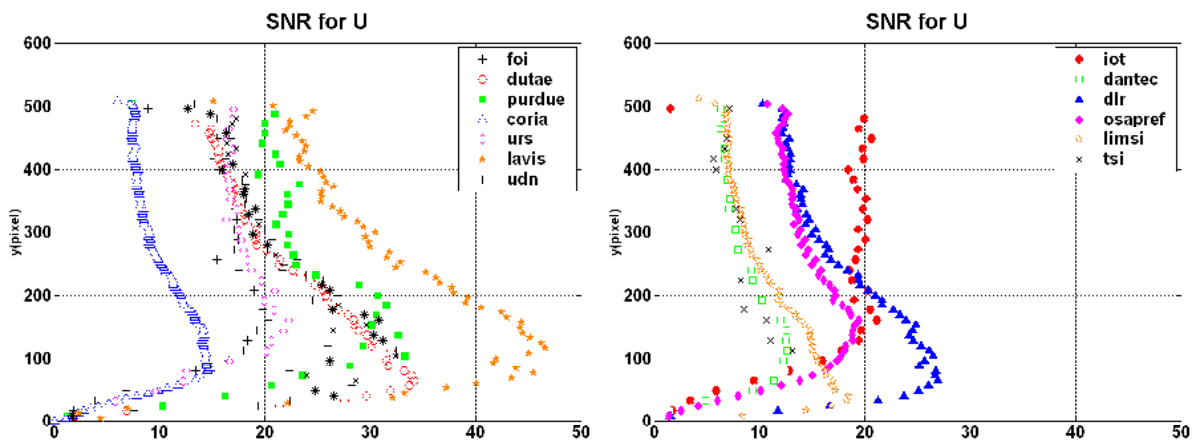
Figure 19 Turbulence signal to noise ratio obtained by a) the first and b) the second PIV group.
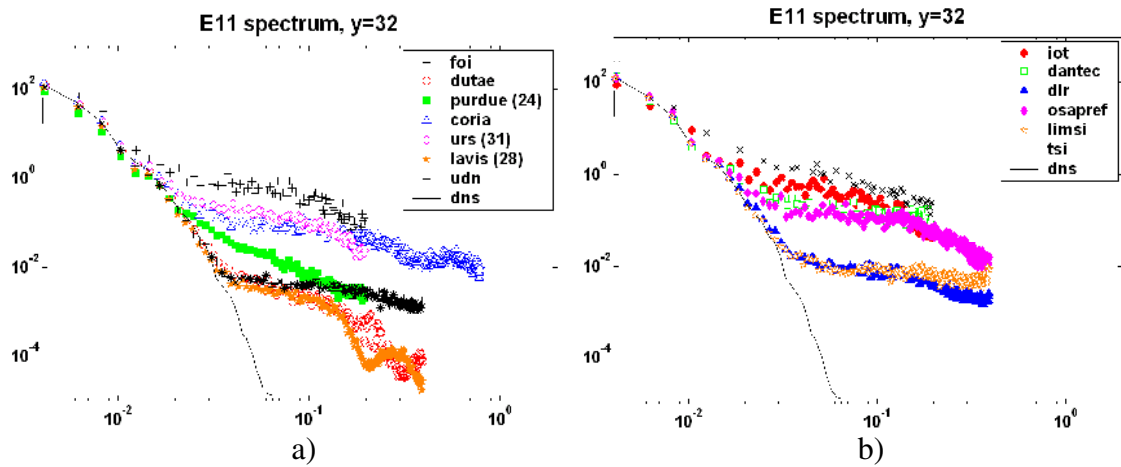
Figure 20 Spectrum of the streamwise velocity fluctuations obtained by a) the first and b) the second PIV group.
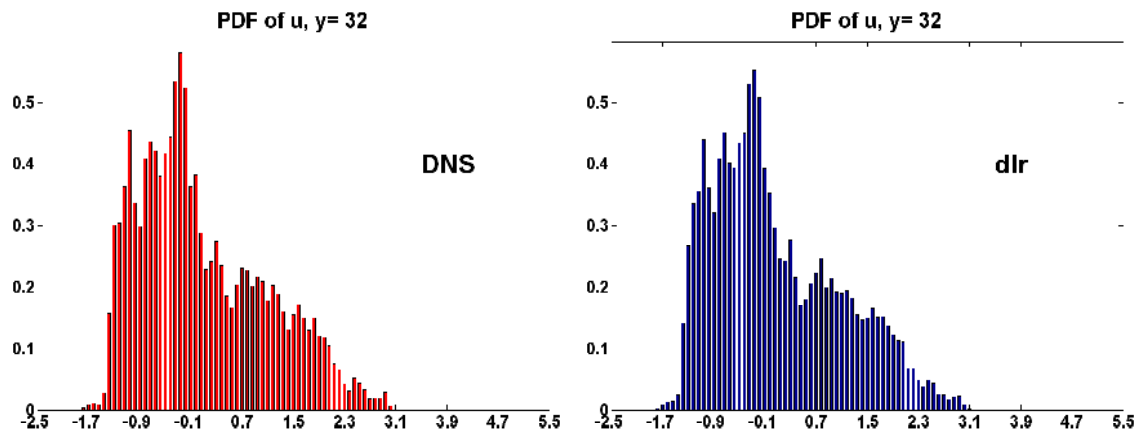

Figure 21 : Probability density function of the streamwise velocity fluctuations at y+ = 32. Comparison between DNS and the results obtained by DLR.
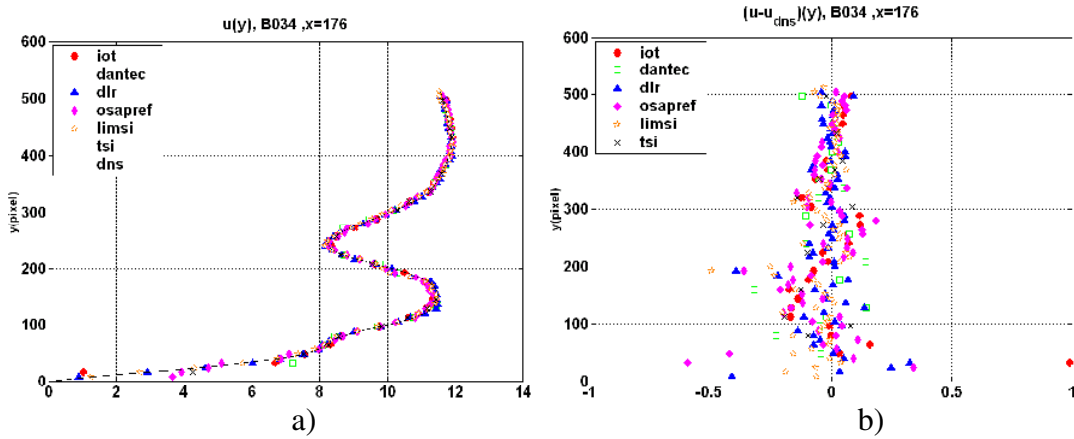
Figure 22 Example of a) instantaneous streamwise velocity profile and b) difference to the DNS obtained by the second PIV group.
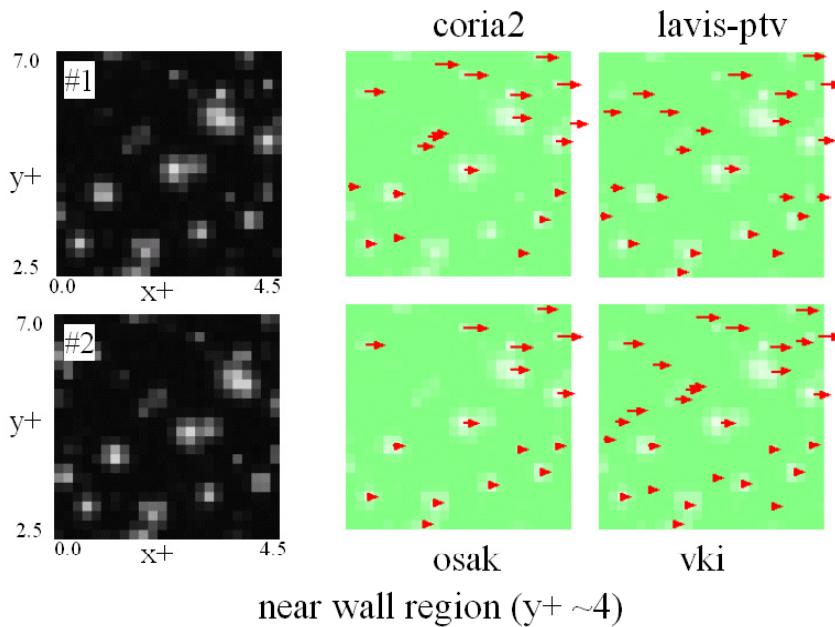
Figure 23 Instantaneous velocity vectors obtained by the PTV group in the near wall region (y+=2.5~7.0).
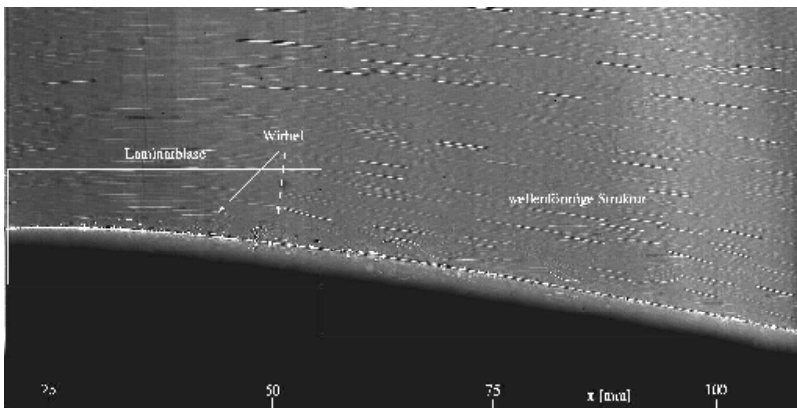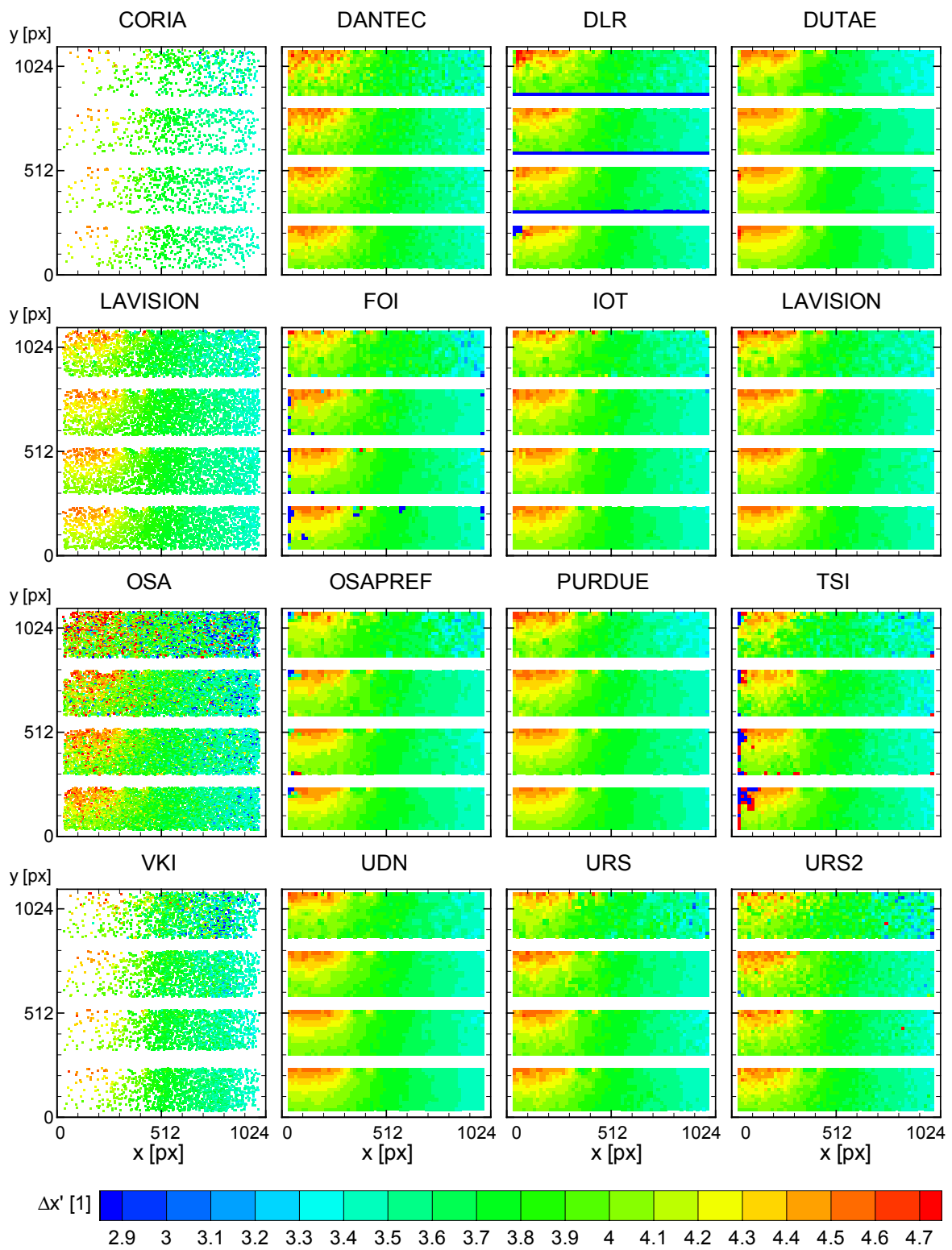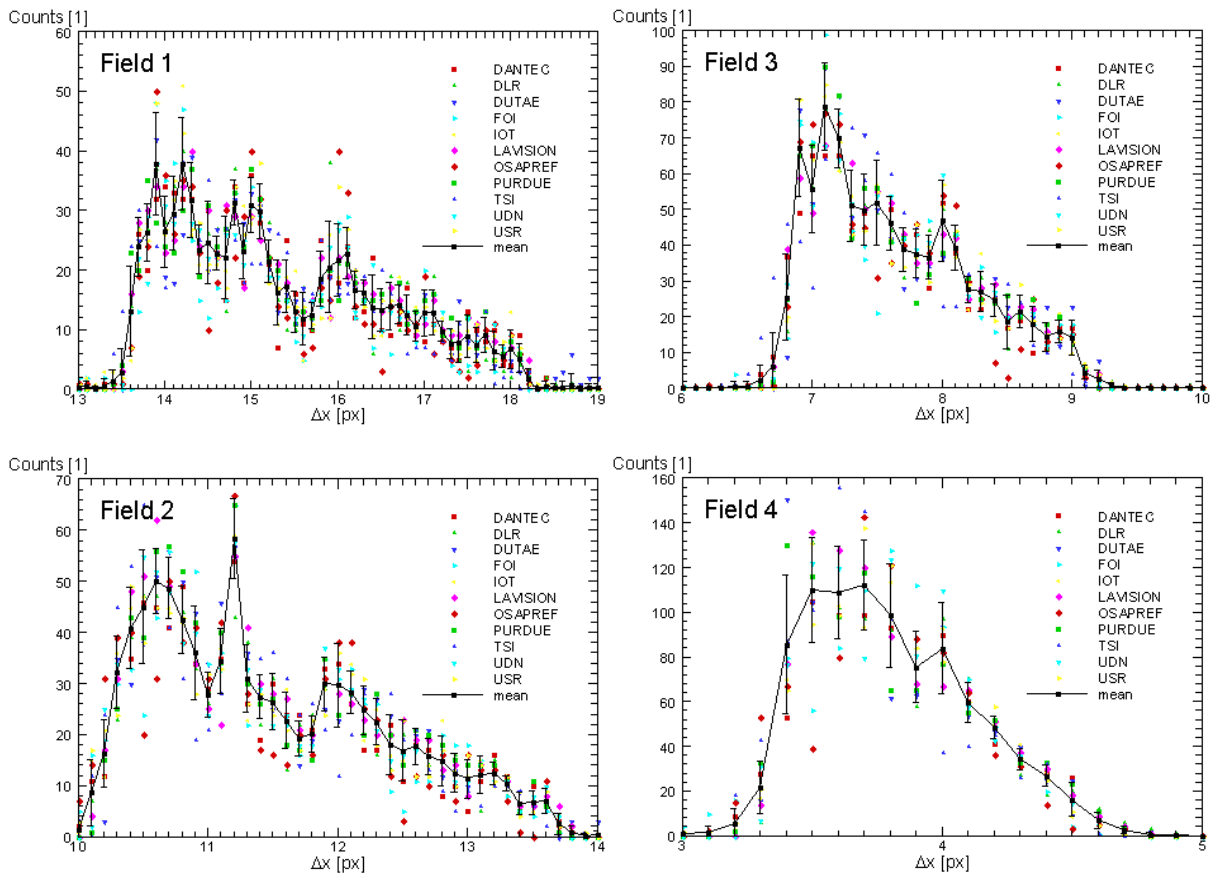
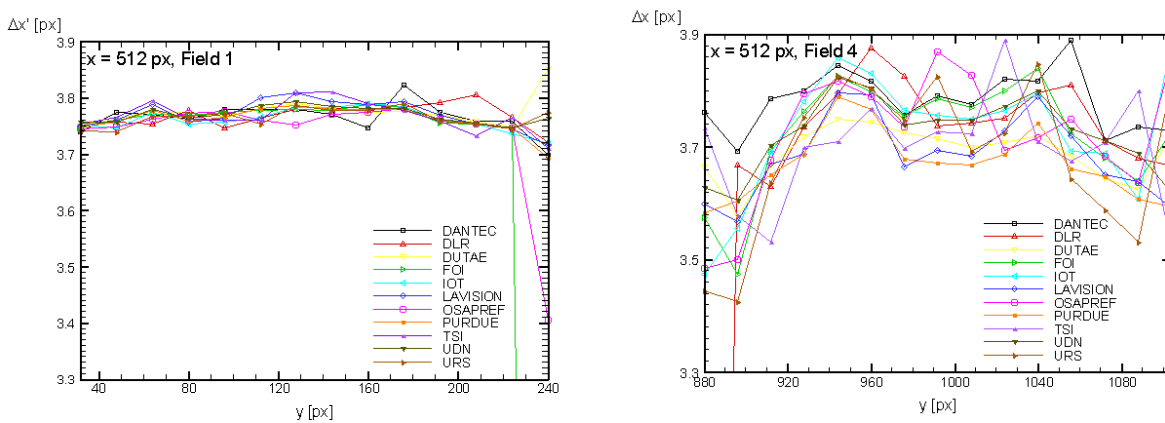**Figure 24 Sample of image used for test case C.**

Figure 25 Comparison of the normalised particle image displacement in x direction for all teams.

Figure 26 Histogram of the particle image displacement in x direction for all teams and fields along with the average and rms values.

Figure 27 Normalised particle image displacement in x direction along the y axis at x=512. The difference between the right graphs and the left ones indicate the measurement error for each team.